Synaptopodin-associated ribosomal hubs regulate lesion-induced homeostatic plasticity at hippocampal mossy fiber synapses

Pia Kruse[1], Andreas Vlachos[1,2,3,§], Maximilian Lenz[1,§]

[1]Department of Neuroanatomy, Institute of Anatomy and Cell Biology, Faculty of Medicine, University of Freiburg, Freiburg, Germany.

[2]Center for Basics in Neuromodulation (NeuroModulBasics), Faculty of Medicine, University of Freiburg, Freiburg, Germany.

[3]Center BrainLinks-BrainTools, University of Freiburg, Freiburg, Germany.

[§]Correspondence to andreas.vlachos@anat.uni-freiburg.de and maximilian.lenz@anat.uni-freiburg.de, Department of Neuroanatomy, Institute of Anatomy and Cell Biology, Faculty of Medicine, University of Freiburg, 79104 Freiburg, Germany

Keywords: homeostatic plasticity, denervation, synaptopodin, local protein synthesis

ABSTRACT

Neurological diseases can lead to the denervation of brain regions caused by demyelination, traumatic injury or cell death. Nevertheless, the molecular and structural mechanisms underlying lesion-induced reorganization of denervated brain regions are a matter of ongoing investigation. In order to address this issue, we performed an entorhinal cortex lesion (ECL) in mouse organotypic entorhino-hippocampal tissue cultures of both sexes and studied denervation-induced homeostatic plasticity of mossy fiber synapses, which connect dentate granule cells with CA3 pyramidal neurons and play important roles in spatial learning. Partial denervation caused a homeostatic strengthening of excitatory neurotransmission in dentate granule cells (GC), in CA3 pyramidal neurons, and their direct synaptic connections as revealed by paired recordings (GC-to-CA3). These functional changes were accompanied by ultrastructural reorganization of mossy fiber synapses, which regularly contain the plasticity-related protein synaptopodin and the spine apparatus organelle. We demonstrate that the spine apparatus organelle and its associated protein synaptopodin assemble ribosomes in close proximity to synaptic sites and unravel a synaptopodin-related transcriptome, which can be linked to the expression of homeostatic synaptic plasticity. Notably, synaptopodin-deficient tissue preparations that lack the spine apparatus organelle, failed to express homeostatic adjustments. Hence, synaptopodin and the spine apparatus organelle form local protein synthesis hubs that are essential for mediating lesion-induced homeostatic synaptic plasticity.

INTRODUCTION

Denervation is a common feature of various neurological diseases, which are accompanied by neuronal cell death, demyelination or traumatic injury (Mesulam et al., 2019). As a result of the loss-of-input in otherwise healthy brain regions, complex reorganizational processes of neural circuits have been described. Among them, homeostatic synaptic plasticity has been established as an adaptive process of synaptic features that aims at compensating for perturbations of network activity (Turrigiano, 2012; Vitureira et al., 2012; Turrigiano, 2017). Specifically, compensatory excitatory synaptic strengthening upon denervation or activity deprivation has been reported (Turrigiano et al., 1998). Although homeostatic synaptic plasticity has been recognized as a local mechanism that can occur at distinct dendritic regions, the mechanisms that mediate dendritic autonomy in maintaining homeostasis remain widely unknown.

The hippocampal network is a crucial structure in memory acquisition. Here, the excitatory connection between dentate granule cells and CA3 pyramidal cells, i.e., the hippocampal mossy fiber synapse, has been demonstrated to play a crucial role in memory formation, maintenance and retrieval (Weng et al., 2018). Although numerous studies have addressed the unique plasticity features of this synapse (e.g. the onset of synaptic homeostasis and detonating transmission; (Lee et al., 2013)) and its impact on memory and behavior, no studies have addressed whether lesion-induced homeostatic synaptic plasticity occurs at this synapse when the main cortical excitatory input is affected. In this context, organotypic tissue cultures of the entorhino-hippocampal complex provide the opportunity to study synaptic transmission at hippocampal mossy fiber synapses in steady-state condition (Maus et al., 2020). Due to the laminated cortico-hippocampal input, the *in vitro* entorhinal cortex lesion (ECL) has been established as a model for the partial denervation of hippocampal neural circuits (Prang et al., 2003; Vlachos et al., 2012a; Vlachos et al., 2012c; Lenz et al., 2019).

In this study we used an entorhinal cortex lesion (ECL) of organotypic entorhino-hippocampal tissue cultures to study homeostatic adaptations in the dentate gyrus and CA3 network upon partial denervation. We provide evidence that partial denervation leads to excitatory synaptic strengthening in both dentate granule cells and CA3 pyramidal neurons. Using paired whole-cell patch-clamp recordings, we demonstrate changes in the synaptic transmission at hippocampal mossy fiber synapses. These changes are accompanied by an ultrastructural reorganization of the spine apparatus organelle, which has previously been linked to synaptic plasticity (Deller et al., 2003; Jedlicka et al., 2009; Vlachos et al., 2009; Vlachos et al., 2013; Korkotian et al., 2014; Jedlicka and Deller, 2017; Maggio and Vlachos, 2018; Lenz et al., 2021b; Lenz et al., 2021a). We demonstrate that synaptopodin and the spine apparatus organelle form ribosomal hubs that are linked to homeostatic plasticity-related local protein synthesis (Sutton et al., 2006). Consequently, synaptopodin-deficient tissue cultures, which lack the spine apparatus organelle, showed deficits in the expression of homeostatic changes in excitatory neurotransmission and regional trancriptomes upon ECL. We therefore conclude, that the spine

apparatus organelle forms plastic local protein synthesis hubs that contribute to homeostatic synaptic adjustments upon partial denervation.

72 **MATERIALS AND METHODS**

73 **Ethics statement**

74 Mice were maintained in a 12 h light/dark cycle with food and water available ad libitum. Every effort
75 was made to minimize distress and pain of animals. All experimental procedures were performed
76 according to German animal welfare legislation and approved by the appropriate animal welfare
77 committee and the animal welfare officer of Albert-Ludwigs-University Freiburg, Faculty of Medicine
78 (X-17/07K, X-17/09K, X-21/01B).

79 **Preparation of tissue cultures**

80 Entorhino-hippocampal tissue cultures were prepared at postnatal day 3-5 from C57BL/6J (wildtype,
81 Synpo$^{+/+}$) and B6.129-Synpo^{tm1Mndl}/Dllr [Synpo$^{-/-}$, (Deller et al., 2003; Lenz et al., 2021b; Lenz et al.,
82 2021a)] mice of either sex as previously described (Del Turco and Deller, 2007). Cultivation medium
83 contained 50% (v/v) MEM, 25% (v/v) basal medium eagle, 25% (v/v) heat-inactivated normal horse
84 serum, 25 mM HEPES buffer solution, 0.15% (w/v) bicarbonate, 0.65% (w/v) glucose, 0.1 mg/ml
85 streptomycin, 100 U/ml penicillin, and 2 mM glutamax. The pH was adjusted to 7.3. All tissue cultures
86 were allowed to mature for at least 18 days in a humidified atmosphere with 5% CO_2 at 35°C.
87 Cultivation medium was replaced 3 times per week.

88 **Entorhinal cortex lesion (ECL)**

89 The entorhinal cortex of mature slice cultures (≥18 days *in vitro*) was transected with a sterile scalpel
90 from the rhinal to the hippocampal fissure to achieve a complete lesion of the perforant path. Except for
91 the lesion-induced partial denervation of the hippocampus, cytoarchitecture of both the hippocampus
92 and the entorhinal cortex remained unchanged.

93 **Whole-cell patch-clamp recordings**

94 Whole-cell patch-clamp recordings were carried out at 35°C (3-6 neurons per culture). The bath solution
95 contained (in mM) 126 NaCl, 2.5 KCl, 26 $NaHCO_3$, 1.25 NaH_2PO_4, 2 $CaCl_2$, 2 $MgCl_2$, and 10 glucose
96 (aCSF) and was oxygenated continuously (5% CO_2 / 95% O_2). Patch pipettes contained (in mM) 126
97 K-gluconate, 10 HEPES, 4 KCl, 4 ATP-Mg, 0.3 GTP-Na_2, 10 PO-Creatine, 0.3% (w/v) biocytin (pH
98 7.25 with KOH, 290 mOsm with sucrose), having a tip resistance of 4-6 MΩ. Pyramidal neurons were
99 visually identified using a LN-Scope (Luigs & Neumann) equipped with an infrared dot-contrast and a
100 40x water-immersion objective (NA 0.8; Olympus). Spontaneous excitatory postsynaptic currents
101 (sEPSCs) of both dentate granule cells and CA3 pyramidal neurons were recorded in voltage-clamp
102 mode at a holding potential of −70 mV. Series resistance was monitored before and after each recording
103 and recordings were discarded if the series resistance reached ≥ 30 MΩ. For recording of intrinsic
104 cellular properties in current-clamp mode, pipette capacitance of 2.0 pF was corrected and series
105 resistance was compensated using the automated bridge balance tool of the MultiClamp commander. I-

106 V-curves were generated by injecting 1 s square pulse currents starting at −100 pA and increasing in 10
107 pA steps until +500 pA current injection was reached (sweep duration: 2 s).

108 **Paired whole-cell patch-clamp recordings of hippocampal mossy fiber synapses**

109 Action potentials were generated in the presynaptic dentate granule cell by 5 ms square current pulses
110 (1 nA). For connectivity analysis, 5 action potentials were applied at 20 Hz respectively (inter-sweep-
111 interval: 10 sec; at least 30 repetitions), while recording unitary excitatory postsynaptic currents
112 (uEPSCs) from CA3 pyramidal cells. Neurons were considered to be connected if > 5 % of action
113 potentials evoked time-locked inward uEPSCs (Vlachos et al., 2012b). Recordings were performed in
114 the presence of (-)-bicuculline-methiodide (10 µM, #ab120108 Abcam) to prevent inhibitory synapse
115 recruitment. Moreover, glutamine (200 µM, #11539876 Gibco) was added to the recording medium to
116 avoid synapse depletion (Tani et al., 2014).

117 **Post-hoc staining and imaging**

118 Tissue cultures were fixed overnight in a solution of 4% (w/v) paraformaldehyde (PFA; in PBS (0.1M,
119 pH 7.4) with 4% (w/v) sucrose). After fixation, cultures were washed in PBS (0.1 M, pH 7.4) and
120 consecutively incubated for 1 h with 10% (v/v) normal goat serum (NGS) in 0.5% (v/v) Triton X-100
121 containing PBS to reduce nonspecific staining. For post-hoc visualization of patched granule cells and
122 CA3 pyramidal cells, Streptavidin Alexa Fluor 488 (Streptavidin A488, 1:1000; #S32354 Invitrogen)
123 was added to the incubation solution. DAPI nuclear stain (1:5000 in PBS for 10 minutes; #62248
124 Thermo Scientific) was used to visualize cytoarchitecture. Cultures were washed, transferred onto glass
125 slides and mounted for visualization with DAKO anti-fading mounting medium (#S302380-2, Agilent).

126 **Transmission electron microscopy**

127 Wildtype (Synpo$^{+/+}$) and Synpo$^{-/-}$ tissue cultures were fixed in 4 % paraformaldehyde (w/v) and 2 %
128 glutaraldehyde (w/v) in 0.1 M phosphate buffer (PB) overnight and washed for 1 hour in 0.1 M PB.
129 After fixation, tissue cultures were sliced with a vibratome and the slices were incubated with 1 %
130 osmium tetroxide for 20 min in 5 % (w/v) sucrose containing 0.1 M PB. The slices were washed 5 times
131 for 10 min in 0.1 M PB and washed in graded ethanol [10 min in 10 % (v/v) and 10 min in 20 % (v/v)].
132 The slices were then incubated with uranyl acetate [1 % (w/v) in 70 % (v/v) ethanol)] overnight and
133 were subsequently dehydrated in graded ethanol 80 % (v/v), 90 % (v/v) and 98 % (v/v) for 10 min.
134 Finally, slices were incubated with 100 % (v/v) ethanol twice for 15 min followed by two 15 min washes
135 with propylene oxide. The slices were then transferred for 30 min in a 1:1 mixture of propylene oxide
136 with durcupan and then for 1 hour in durcupan. The durcupan was exchanged with fresh durcupan and
137 the slices were transferred to 4 °C overnight. The slices were then embedded between liquid release-
138 coated slides and coverslips. Cultures were re-embedded and ultrathin sections were collected on copper
139 grids. Electron microscopy was performed at a LEO 906E microscope (Zeiss) at 4646x magnification.

140 **Regional mRNA library preparations and transcriptome analysis**

141 RNA library preparations for transcriptome analysis were performed using the NEBNext® Single
142 Cell/Low Input RNA Library Prep Kit for Illumina® (New England Biolabs, #E6420) according to the
143 manufacturer's instructions. Briefly, isolation of the dentate gyrus and CA3 area from individual tissue
144 cultures was performed using a scalpel. One isolated dentate gyrus or CA3 area respectively was
145 transferred to 7.5 µl lysis buffer (supplemented with murine RNase inhibitor) and homogenized using a
146 pestill. Samples were centrifuged for 30 seconds at 10,000g and 5 µl of supernatant were collected from
147 individual samples and further processed. After cDNA synthesis, cDNA amplification was performed
148 according to the manufacturer's protocol. cDNA yield was consecutively analyzed by a High Sensitivity
149 DNA assay on a Bioanalyzer instrument (Agilent). cDNA amount was adjusted to 10 ng for further
150 downstream applications. After fragmentation and adaptor ligation, dual index primers (New England
151 Biolabs, #E7600S) were ligated in a library amplification step using 10 PCR cycles. Libraries were
152 finally cleaned up with 0.8X SPRI Beads following a standard bead purification protocol. Library purity
153 and size distribution was assessed with a High Sensitivity DNA assay on a Bioanalyzer instrument
154 (Agilent). We quantified the libraries using the NEBNext Library Quant Kit for Illumina (New England
155 Biolabs, #E7630) based on the mean insert size provided by the Bioanalyzer. A 10 nM sequencing pool
156 (120 µl in Tris-HCl, pH 8.5) was generated for sequencing on the NovaSeq6000 sequencing platform
157 (Illumina; service provided by CeGaT GmbH, Tübingen, Germany). We performed a paired-end
158 sequencing with 101 bp read length. Data analysis was performed at the Galaxy platform (usegalaxy.eu).
159 All files contained more than 10 M high-quality reads (after mapping to the reference genome; mm10)
160 having at least a phred quality of 30 (>90% of total reads).

161 **Synaptopodin co-Immunoprecipitation (SP-coIP) and RT-qPCR analysis**

162 Six tissue cultures per biological replicate were washed in coIP-solution and dounce homogenized on
163 ice in a solution containing (150 µl per sample, coIP-solution, in mM): 10 HEPES, 120 NaCl, 0.05%
164 (v/v) NP-40, cOmplete protease inhibitor (Roche, according to manufacturers' instructions), murine
165 RNase inhibitor (1:1000, New England Biolabs, #M0314) and cycloheximide (0.5 mg/ml, Sigma
166 Aldrich, #C-4859). Input was precleared twice with protein A beads (10 µl per 100 µl
167 sample/supernatant) to reduce unspecific binding. Protein A beads (10 µl, New England Biolabs,
168 #S1425) were washed twice in coIP-solution and consecutively incubated for 1 hour at 4°C with an anti-
169 Synaptopodin antibody (rabbit anti-Synaptopodin, Synaptic Systems, #163002). Beads were carefully
170 washed twice to remove unbound antibodies and incubated for 1 hour with the precleared supernatant
171 ('input') at 4°C with head-over-tail rotation. 10 µl of the precleared supernatant were kept as input
172 control. After incubation, beads were washed twice with coIP-solution and finally dissolved in RNA
173 protection buffer (New England Biolabs). RNA was released from the beads through Protein K lysis
174 (Monarch® Total RNA Miniprep Kit; #T2010S New England Biolabs). After lysis, beads were removed

175 from the solution in a magnetic rack and the RNA containing supernatant was transferred to fresh tubes.
176 RNA isolation on coIP- and input-samples was then performed according to the manufacturer's
177 instructions. RNA content was determined using the Agilent RNA 6000 Pico Kit (#5067-1513 Agilent)
178 with a 2100 Bioanalyzer (#G2939BA Agilent). For RT-qPCR analysis, purified RNA was consecutively
179 reverse transcribed (RevertAid RT Kit; #K1691 Thermo Scientific). cDNA was diluted in water to a
180 final concentration of 0.2 ng/µl. RT-qPCR was performed using a C1000 Touch Thermal Cycler (BIO-
181 RAD) and the CFX 384 Real-Time PCR system (BIO-RAD). 0.9 ng target cDNA diluted in TaqMan
182 Gene Expression Master Mix (Applied Biosystems #4369016) were amplified using standard TaqMan
183 Gene Expression Assays (Applied Biosystems; Assay-IDs: Gapdh: Mm99999915_g1; Gria1:
184 Mm00433753_m1). RNA library preparations for Synpo-related transcriptome analysis were performed
185 using the NEBNext® Single Cell/Low Input RNA Library Prep Kit for Illumina® (New England Biolabs,
186 #E6420) according to the manufacturer's instructions. We quantified the libraries using the NEBNext
187 Library Quant Kit for Illumina (New England Biolabs, #E7630) based on the mean insert size provided
188 by the Bioanalyzer. A 10 nM sequencing pool (120 µl in Tris-HCl, pH 8.5) was generated for sequencing
189 on the NovaSeq6000 Sequencing platform (Illumina; service provided by CeGaT GmbH, Tübingen,
190 Germany). We performed a paired-end sequencing with 151 bp read length. Data analysis was
191 performed at the Galaxy platform (usegalaxy.eu). All files contained more than 10 M high-quality reads
192 (after mapping to the reference genome; mm10) having at least a phred quality of 30 (>90% of total
193 reads).

194 **Quantification and statistics**

195 Electrophysiological data were analyzed using pClamp 10.7 (Axon Instruments) and MiniAnalysis
196 (Synaptosoft) software. The fraction of action potentials followed by time-locked excitatory
197 postsynaptic current responses was considered as synaptic response rate. uEPSC amplitude was assessed
198 in uEPSCs from successfully transmitted action potentials as well as the mean amplitude of all
199 successfully evoked postsynaptic responses. In order to ensure analysis of time-locked unitary
200 responses, events were included if > 5% of presynaptic pulses were successfully transmitted for each
201 pulse respectively. For individual pulses in pulse trains that caused ≤ 5% successfully transmitted
202 events, response rate was set to '0'. EPSC properties were analyzed using the automated template search
203 tool for event detection. In order to perform a hierarchical analysis of sEPSCs, all events of a recorded
204 cell were sorted based on their peak amplitude. Events above the 50th percentile therefore correspond to
205 all events above the median amplitude of events. Input resistance was calculated for the injection of –
206 100 pA current at a time frame of 200 ms with a maximum distance to the initial hyperpolarization.
207 Resting membrane potential was calculated as the mean baseline value. AP detection was performed
208 using the input-output curve threshold search event detection tool, and the AP frequency was assessed
209 by the number of APs detected during the respective current injection time (1s).

RT-qPCR data were analyzed as previously described (Lenz et al., 2020) with the Bio-Rad CFX Maestro 1.0 software package using the ΔΔCq method with Gapdh as reference gene. Values were normalized to the mean value of the respective control group.

Electron microscopy images were saved as TIF-files and analyzed using the ImageSP Viewer software (http://e.informer.com/sys-prog.com). Ultrastructural features were analyzed by an investigator blind to experimental conditions in randomly selected mossy fiber terminals from electron micrographs of the stratum lucidum in non-lesioned and lesioned wildtype tissue cultures.

RNA sequencing data were uploaded to the Galaxy web platform (public server: usegalaxy.eu; (Goecks et al., 2010; Afgan et al., 2018; Galaxy, 2022)) and transcriptome analysis was performed using the Galaxy platform in accordance with the reference-based RNA-seq data analysis tutorial (Batut et al., 2021). Adapter sequencing, low quality, and short reads were removed via the CUTADAPT tool (Galaxy version 3.5+galaxy0). Reads were mapped using RNA STAR (Galaxy version 2.7.8a+galaxy0) with the mm10 full reference genome (Mus musculus). The evidence-based annotation of the mouse genome (GRCm38), version M25 (Ensembl 100), served as gene model (GENCODE). For an initial assessment of gene expression, unstranded FEATURECOUNT (Galaxy version 2.0.1+galaxy2) analysis was performed from RNA STAR output. Only samples that contained >60% uniquely mapping reads (feature: "exon") were considered for further analysis. Statistical evaluation was performed using DESeq2 (Galaxy version 2.11.40.7+ galaxy1) with "pathway integrity" (ECL experiments) or "coIP" (synaptopodin-coIP experiments) as the primary factor that might affect gene expression. Genes with a low number of mean reads (< 300 BaseMean) were excluded from further analysis. Genes were considered as differentially expressed or enriched if the adjusted p-value was < 0.05. Data visualization was performed according to a modified version of a previously published workflow (Reimand et al., 2019). A ranked list for the gene set enrichment analysis was generated based on Wald-Stats from the DeSeq2 output. For the consecutive gene set enrichment analysis, we have used the GSEA software package ((Mootha et al., 2003; Subramanian et al., 2005); BROAD institute; version GSEA_4.2.1) with integrated MSigDB gene sets. Enrichment maps were built using cytoscape ((Shannon et al., 2003); version 3.9.0) with the EnrichmentMap application. Further functional enrichment analyses were performed using g:Profiler (version e107_eg54_p17_bf42210) with g:SCS multiple testing correction method applying significance threshold of 0.05 (Raudvere et al., 2019). Gene sets with 100-500 terms were considered for illustration. Heatmaps were generated based on z-scores of the normalized count table.

Data were statistically analyzed using GraphPad Prism 7 (GraphPad software, USA). All values represent mean ± standard error of the mean. For statistical comparison of two experimental groups, a Mann-Whitney test was employed. EPSC amplitude/frequency plots and AP-frequency plots were statistically assessed by the repeated measure (RM) two-way ANOVA test with Sidak's (two groups) multiple comparisons test. uEPSC amplitude values from individual cells were stacked in subcolumns and the pulse number was defining tabular rows (COLUMN factor: pathway integrity, genetic

background; ROW factor: EPSC amplitude bin or current injection). P-values < 0.05 were considered statistically significant (*p < 0.05, **p < 0.01, ***p < 0.001); results that did not yield significant differences are designated 'ns'. Statistical differences in XY-plots were indicated in the legend of the figure panels (*) when detected through multiple comparisons, irrespective of their localization and the level of significance. In the text and figures, values represent the mean ± standard error of the mean (s.e.m.).

Data availability

Sequencing data have been deposited in the Gene Expression Omnibus (GEO) repository (accession number: GSE216509). Original data are available from the authors upon reasonable request.

Digital illustrations

Confocal image stacks were stored as TIF files. Figures were prepared using the ImageJ software package (https://imagej.nih.gov/ij/) and Photoshop graphics software (Adobe, San Jose, CA, USA). Image brightness and contrast were adjusted.

RESULTS

Entorhinal cortex lesion leads to homeostatic synaptic plasticity in both dentate granule cells and CA3 pyramidal neurons

Entorhinal cortex lesion was performed in mature tissue cultures to achieve a complete dissection of the perforant path leading to a partial denervation of both dentate granule cells and CA3 pyramidal neurons (Figure 1A). Spontaneous excitatory postsynaptic currents (sEPSCs) were recorded from dentate granule cells and CA3 pyramidal neurons in non-lesioned control and lesioned tissue cultures (3 days post entorhinal cortex lesion, 3dp ECL) to assess denervation-induced effects on excitatory neurotransmission (Figure 1B). As previously described [e.g., (Vlachos et al., 2012c; Lenz et al., 2019)], partial denervation caused a strengthening of excitatory synapses in dentate granule cells, i.e., a significant increase in both the mean sEPSC amplitude and half width as well as the mean sEPSC area (Figure 1C). Percentile analysis revealed that the lesion-induced increase in sEPSC amplitudes is evident when comparing the 50% biggest events in both groups while no effect was observed when comparing smaller events (Figure 1D). Notably, a significant upregulation in the mean sEPSC frequency was observed after lesion (Figure 1E) that resulted from an increased abundance of high amplitude sEPSCs as revealed by the amplitude/frequency-plot (Figure 1F).

Next, we examined excitatory neurotransmission in CA3 pyramidal neurons in non-lesioned and lesioned cultures (3dp ECL; Figure 1G-J). Again, a significant increase in both the mean sEPSC amplitude and area was observed in CA3 cells from lesioned cultures indicating a denervation-induced excitatory synaptic strengthening (Figure 1G). Notably, the mean sEPSC half width remained unchanged. In the sEPSC amplitude percentile analysis, excitatory synaptic strengthening seems to be restricted to the high amplitude events (Figure 1H). Moreover, the mean sEPSC frequency remained unchanged upon ECL (Figure 1I), which resulted from an increase in the abundance of high amplitude events (in the sEPSC amplitude range from 80-110 pA, RM two-way ANOVA followed by Sidak's multiple comparisons test) at the expense of small amplitude events (Figure 1J). We therefore conclude that ECL leads to a homeostatic increase in excitatory neurotransmission in both dentate granule cells and CA3 pyramidal neurons.

Partial denervation does not cause changes in intrinsic cellular properties

Passive and active membrane properties were assessed in both dentate granule cells (Figure 2A-C) and CA3 pyramidal neurons (Figure 2D-F) to test for homeostatic adaptations of intrinsic cellular properties upon lesion. In dentate granule cells no changes in passive membrane properties (Figure 2A), i.e., the resting membrane potential (RMP) and the input resistance as well as the input-output curve dynamics were observed (Figure 2B). Additionally, the action potential frequency of dentate granule cells was similar in lesioned and non-lesioned cultures (Figure 2C). Noteworthy, RMP assessment confirmed the mature state of the recorded dentate granule cells [c.f. (Strehl et al., 2018)].

295 Concerning CA3 pyramidal neurons, neither the passive membrane properties (Figure 2D) – including
296 input-output curve dynamics (Figure 2E) – nor the active properties (Figure 2F) were changed. Based
297 on these results, we conclude that intrinsic cellular properties were stable following denervation in both
298 tested cell types of the hippocampal network.

299 **Entorhinal cortex lesion induces changes in synaptic transmission at hippocampal mossy fiber**
300 **synapses**

301 Hippocampal mossy fiber synapses have previously been linked to learning processes and memory
302 formation (Lipp et al., 1988; Vandael et al., 2020). Concerning their synaptic features, they have been
303 described as synapses that generate large postsynaptic currents upon activation (Henze et al., 2002b).
304 Given that our results demonstrate changes in both investigated regions, which additionally hint towards
305 a preferential lesion-related plasticity induction in readily strong synapses at CA3 pyramidal neurons,
306 we next assessed the features of synaptic transmission at hippocampal mossy fiber synapses.
307 Therefore, we performed paired whole-cell patch-clamp recordings of individual dentate granule cells
308 and CA3 pyramidal neurons in organotypic tissue cultures (Figure 3A). To test for synaptic connections,
309 5 consecutive action potentials at 20 Hz frequency were elicited in dentate granule cells (Figure 3B).
310 Unitary excitatory postsynaptic currents (uEPSCs) were monitored in CA3 pyramidal neurons in non-
311 lesioned and lesioned tissue cultures. We found that a train of presynaptic action potentials in connected
312 neurons induced a robust facilitation of postsynaptic responses in both postsynaptic response rate and
313 uEPSC amplitude under baseline conditions (Figure 3B-D). Notably, the response rate to the first
314 presynaptic action potential, which is the number of presynaptic action potentials that generate a
315 postsynaptic response, was low in non-lesioned cultures (~3%; Figure 3C). In lesioned cultures,
316 however, a significant increase in the synaptic reliability for the first two pulses was observed. For the
317 last three pulses in one train of stimulation, averaged synaptic response rate levels became similar
318 (Figure 3C). Moreover, the uEPSC amplitude was significantly increased in response to the individual
319 pulses 3 days after ECL (Figure 3D). This novel approach of GC-to-CA3 paired recordings in the steady-
320 state environment of organotypic tissue cultures provided evidence that synaptic transmission at
321 hippocampal mossy fiber synapses is a target for lesion-induced remodeling of hippocampal networks.

322 **Synaptopodin and the spine apparatus organelle form dendritic ribosomal hubs that are**
323 **associated with excitatory synapse related mRNAs**

324 Hippocampal mossy fiber synapses show a complex organization of their pre- and postsynaptic sites.
325 Among these features, a regular occurrence of the spine apparatus organelle, which is a transmission-
326 and plasticity-regulating organelle, has been reported at the postsynaptic site (Chicurel and Harris,
327 1992). Using transmission electron microscopy, a close interaction between ribosomes and the spine
328 apparatus organelle was readily revealed (Figure 4A). We hypothesized that the spine apparatus
329 organelle at its marker protein synaptopodin (Deller et al., 2003) might regulate lesion-induced plasticity

330 at hippocampal mossy fiber synapses by regulating local protein synthesis. To test whether
331 synaptopodin interacts with local translation machineries, i.e., dendritic ribosomes, we performed
332 synaptopodin co-immunoprecipitation (Synpo-coIP) experiments with subsequent RT-qPCR analysis.
333 Using RNA assessment on a Bioanalyzer, we found rRNA peaks in Synpo-coIP experiments whereas
334 no rRNA was detected in bead-only controls (Figure 4B). RT-qPCR analysis (reference gene: Gapdh)
335 from input and Synpo-coIP samples revealed an enrichment of Gria1 mRNA (Figure 4C), which has
336 been linked to synaptopodin-dependent synaptic plasticity (Vlachos et al., 2009) and homeostatic
337 synaptic adjustments (Sutton et al., 2006; Aoto et al., 2008). We therefore conclude, that synaptopodin
338 and the spine apparatus organelle might serve as a ribosomal hub that significantly contributes to
339 plasticity-related local protein synthesis.
340 To further unravel the plasticity-mediating features of synaptopodin and the spine apparatus organelle,
341 we performed a transcriptome analysis of Synpo-coIP enriched mRNA (Figure 4D, extended data table
342 4-1). A considerable amount of mRNAs was enriched after Synpo-coIP compared to input samples (UP;
343 2355 mRNAs; extended data table 4-2). Subsequently, a gene set enrichment analysis (GSEA) was
344 performed to elucidate the functional relevance of synaptopodin-associated mRNAs (Figure 4E).
345 Among others, an enrichment in synapse and actin cytoskeleton-related gene sets was identified. Of
346 note, these data suggest the synaptopodin-dependent assembly of ribosomal hubs that might be
347 dedicated to local protein synthesis at synapses.

348 **Ultrastructural reorganization of the spine apparatus organelle**

349 Previous studies have demonstrated that the ultrastructural organization of the spine apparatus organelle
350 might represent a target for plasticity (Vlachos et al., 2013; Lenz et al., 2021a). To study lesion-induced
351 effects on the ultrastructural organization of the spine apparatus organelle that might interfere with local
352 protein synthesis, we performed transmission electron microscopy of mossy fiber synapses in non-
353 lesioned and lesioned (3dp ECL) entorhino-hippocampal tissue cultures (Figure 4F; c.f., (Vlachos et al.,
354 2013)). No differences in the structural organization of pre- and postsynaptic sites could be detected
355 between the groups (presynapse: mossy fiber perimeter: 11.61 ± 0.4 µm (control; n = 120) vs. 10.88 ±
356 0.35 µm (3dp ECL; n = 90); postsynapse: number of PSDs: 4.91 ± 0.33 (control; n = 120) vs. 4.6 ± 0.27
357 (3dp ECL; n = 90), length of PSDs: 201 nm ± 4.35 (control; n = 589) vs. 201.7 ± 5.42 nm (3dp ECL; n
358 = 414); values indicate mean ± sem, Mann-Whitney test). Nevertheless, a substantial reorganization of
359 the spine apparatus organelle was evident in lesioned cultures 3 days after injury compared to non-
360 lesioned controls (Figure 4G, H). We found an increased number of dense plates in spine apparatus
361 organelles from lesioned cultures (Figure 4G). At the same time the length of individual dense plates
362 was significantly reduced in lesioned cultures (Figure 4H). Therefore, we conclude that the spine
363 apparatus organelle represents a target for lesion-induced changes at hippocampal mossy fiber synapses.

364 **The synaptopodin-associated transcriptome remains stable upon lesion**

365 Given the ultrastructural reorganization of the spine apparatus organelle, we next tested whether the
366 composition of the synaptopodin-associated transcriptome changed in lesioned networks 3dp ECL.
367 Therefore, a differential mRNA enrichment analysis was performed in Synpo-coIP and their respective
368 input RNA samples from lesioned and non-lesioned wildtype cultures (Figure 5). In mRNA libraries
369 prepared from input RNA samples, we found a considerable amount of differentially expressed genes
370 upon ECL (extended data table 5-1). In contrast, a limited amount of mRNAs were differentially
371 enriched upon ECL in Synpo-coIP samples (extended data table 5-2). We therefore conclude that the
372 composition of the synaptopodin-associated transcriptome remains widely stable upon partial
373 denervation.

374 **Synaptopodin-deficient tissue cultures show deficits in homeostatic synaptic plasticity upon**
375 **partial denervation**

376 Based on our ultrastructural analysis, we hypothesized that the reorganization of the spine apparatus
377 organelle might contribute to homeostatic synaptic plasticity at hippocampal mossy fiber synapses. To
378 gain further insights concerning the role of the spine apparatus organelle, we performed experiments in
379 synaptopodin-deficient tissue preparations, which lack the spine apparatus organelle (Figure 6; (Deller
380 et al., 2003)).
381 Synaptopodin-deficient dentate granule cells showed a significant increase in both the mean sEPSC
382 amplitude and area as well as the mean sEPSC half width 3 days following ECL (Figure 6A). In contrast,
383 no changes in the mean sEPSC frequency, which have been observed in wildtype (Synpo$^{+/+}$) cultures,
384 were detected (Figure 6B). Moreover, passive membrane properties remained stable upon lesion in
385 synaptopodin-deficient tissue preparations (Figure 6C).
386 When assessing excitatory neurotransmission onto CA3 pyramidal neurons in lesioned and non-lesioned
387 cultures, no significant changes in the sEPSC event analysis (Figure 6D) or the mean sEPSC frequency
388 (Figure 6E) were observed. Again, passive membrane properties remained unchanged (Figure 6F).
389 Thus, we here provide evidence for deficits in homeostatic synaptic adaptations for both dentate granule
390 cells and CA3 pyramidal neurons in synaptopodin-deficient tissue cultures.
391 We extended these findings with GC-to-CA3 paired whole-cell patch-clamp recordings in
392 synaptopodin-deficient preparations (Figure 6G). In contrast to wildtype cultures, no significant
393 differences in the synaptic reliability could be detected 3 days after ECL (Figure 6H). When analyzing
394 the uEPSC amplitude of successfully transmitted events, surprisingly, we found a significant reduction
395 in the pulse-related uEPSC amplitude in lesioned synaptopodin-deficient preparations (Figure 6I).
396 Notably, excitatory neurotransmission seemed facilitated under baseline conditions as compared to
397 wildtype cultures (Figure 7): In addition to significant changes in sEPSC half width, area and
398 amplitude/frequency-plots (Figure 7 A, B), changes in uEPSCs at mossy fiber synapses were evident in
399 paired recordings (Figure 7 C, D). Hence, synaptopodin-deficient mossy fiber synapses responded in a
400 synaptic depression rather than homeostatic synaptic strengthening after the lesion. These findings

401 demonstrate the role of the postsynaptic spine apparatus organelle on plasticity of mossy fiber synapses.
402 They are consistent with recent work that suggested a role of synaptopodin and the spine apparatus in
403 mediating metaplasticity (Hulme et al., 2014; Lenz et al., 2021b).

404 **Entorhinal cortex lesion causes synaptopodin-dependent changes in the region-specific**
405 **hippocampal transcriptome**

406 To further unravel synaptopodin-dependent changes in hippocampal subfields upon lesion, we
407 performed transcriptome analyses of both the dentate gyrus and the CA3 region in non-lesion and
408 lesioned wildtype (Synpo$^{+/+}$) and synaptopodin-deficient (Synpo$^{-/-}$) cultures (Figure 8). The expression
409 analysis revealed a considerable number of genes that are differentially expressed in both hippocampal
410 regions from wildtype animals (Figure 8A, B). In contrast, synaptopodin-deficient tissue culture
411 preparations showed deficits in the lesion-induced adjustment of gene expression in the CA3 region
412 (Figure 8A). Moreover, wildtype and synaptopodin-deficient tissue preparations showed a genotype
413 dependent gene expression adjustment upon lesion in both regions although a common set of regulated
414 genes has been identified (Figure 8B; for detailed tabular results see extended data tables 8-1, 8-2, 8-3,
415 8-4). We therefore conclude, that synaptopodin might act as a sensor that triggers differential gene
416 expression towards homeostatic adjustments in a region-specific fashion.
417 Unbiased gene set enrichment analysis for all differentially expressed genes (gene ontology – molecular
418 function; GO:MF) from wildtype CA3 samples revealed that ECL caused changes in gene expression
419 related to ubiquitin- and GTP-related signaling (Figure 8C). Additionally, significant enrichments in
420 vesicle-, glia- and synapse-related gene sets were evident (gene ontology – cellular compartment;
421 GO:CC). In order to learn more about lesion-induced differential expression of synaptic gene sets in the
422 CA3 region ("synapse"; GOCC: 0045202), differentially expressed gene lists were filtered according to
423 the content of the respective gene ontology (Figure 8D). We found 153 differentially expressed synaptic
424 genes, which correspond to the strengthening of excitatory neurotransmission at mossy fiber synapses.
425 The same analyses were performed for wildtype DG samples (Figure 8E, F). In addition to changes in
426 ubiquitin- and GTP-related signaling genes, enrichments were seen for actin and transcription factor
427 binding (gene ontology – molecular function; Figure 8E). Moreover, endosome and mitochondria
428 related gene sets were enriched (gene ontology – cellular compartment; GO:CC). Notably, 160
429 differentially expressed synaptic genes were identified (Figure 8F).
430 Therefore, we conclude that the lesion-induced change in the region-specific transcriptome might
431 represent an essential component of homeostatic synaptic plasticity.

432 **DISCUSSION**

433 Denervation is a common phenomenon in numerous medical conditions affecting the central nervous
434 system, which can trigger homeostatic adaptations in neural networks (Vlachos et al., 2012c; Hengen et
435 al., 2013; Lambo and Turrigiano, 2013; Platschek et al., 2016; Barnes et al., 2017; Bissen et al., 2021).
436 In this study, we have unraveled a novel feature of the spine apparatus organelle that crucially
437 contributes to the localized expression of compensatory synaptic changes. In line with previous findings
438 that employed proximity proteomics of synaptopodin (Falahati et al., 2022), we identified a close
439 interaction between synaptopodin and ribosomes. Using synaptopodin co-immunoprecipitation
440 experiments, we elucidated the synaptopodin-related transcriptome, which might contribute to
441 plasticity-related local protein synthesis. Together with findings that indicate interactions between
442 synaptopodin and ER-related proteins (Falahati et al., 2022), we suggest a role for synaptopodin and the
443 spine apparatus organelle as local plasticity hubs near synaptic sites.

444 To study lesion-induced changes in synaptic transmission, we used the *in vitro* model of ECL in
445 organotypic entorhino-hippocampal tissue cultures. After *in vitro* maturation, tissue organization
446 reaches a steady-state that is characterized an *in vivo* like ultrastructural synaptic architecture (Haber et
447 al., 2006; Heller and Rusakov, 2017). In this context, recent work has demonstrated that organotypic
448 hippocampal tissue cultures have intact mossy fiber pathways and synapses (Maus et al., 2020).
449 Moreover, the excitatory cortical input – the perforant path – terminates at distal apical dendrites of
450 dentate granule cells and pyramidal neurons of the ammonic subregions (Frotscher and Heimrich, 1995;
451 Frotscher et al., 1995; Frotscher et al., 1997). Our results provide evidence for homeostatic excitatory
452 synaptic plasticity in both dentate granule cells and CA3 pyramidal neurons upon lesion, which is
453 accompanied by changes in the region-specific transcriptome. Moreover, we here established a novel
454 method to assess synaptic transmission at individual hippocampal mossy fiber synapses – the
455 monosynaptic excitatory contacts between dentate granule cells and CA3 pyramidal neurons – in a
456 steady-state environment by paired whole-cell patch-clamp recordings of connected neurons. In this
457 experimental approach, we identified synaptic transmission at hippocampal mossy fiber synapses as a
458 target for denervation induced synaptic plasticity. In addition, ultrastructural changes in the spine
459 apparatus organelle, which is well established in the regulation of synaptic plasticity (Vlachos et al.,
460 2013; Lenz et al., 2021a), can be observed after ECL. Since homeostatic adaptations on both synaptic
461 and transcriptomic levels were altered in synaptopodin-deficient tissue cultures which lack the spine
462 apparatus organelle, we conclude a crucial role for synaptopodin in mediating, sensing and triggering
463 compensatory synaptic changes.

464 The dentate gyrus/CA3 neural network is an integral component of the memory-associated trisynaptic
465 hippocampal pathway. The hippocampal mossy fiber pathway forms large *en passant* synapses and
466 connects one individual granule cell to a limited number of CA3 pyramidal neurons (Acsady et al.,
467 1998). Both regions receive cortical input – the perforant path – from entorhinal layer II stellate cells
468 that can induce, promote and modulate information processing in hippocampal subregions. Moreover,

469 this pathway is a well-established target for various diseases; among them traumatic, inflammatory and
470 neurodegenerative conditions like Alzheimer's disease (AD; (Thal et al., 2000; Robinson et al., 2014)).
471 Here, we demonstrate that both dentate granule cells and CA3 pyramidal neurons express synaptic
472 plasticity upon partial denervation, which might interfere with information processing.
473 The expression of synaptic plasticity in the hippocampal neural circuit is involved in crucial aspects of
474 normal brain function, such as learning and memory. The hippocampal mossy fiber synapse has been
475 linked to distinct forms of memory acquisition and retrieval (Marr, 1971; Hunsaker et al., 2008).
476 Specifically, activity-dependent structural and functional changes in synaptic features have been found
477 to encode distinct input patterns for a prolonged period of time (Lee et al., 2013; Vandael et al., 2020).
478 Notably, alterations in hippocampal mossy fiber transmission have been reported in animal models of
479 Alzheimer's disease (AD) and aging related cognitive decline (Villanueva-Castillo et al., 2017; Viana
480 da Silva et al., 2019) where a particular loss in cortical input pathways onto hippocampal neurons can
481 be found. Nevertheless, it remains unclear if the lesion-induced synaptic response deteriorates cognitive
482 performance. Given that (1) homeostatic synaptic plasticity is altered in synaptopodin-deficient tissue
483 preparations and (2) alterations in synaptopodin expression have been linked to cognitive decline
484 (Wingo et al., 2019), we suggest that synaptopodin-mediated homeostasis aims at maintaining proper
485 network function.
486 Recently, characteristic features of transmission and stabilizing factors at hippocampal mossy fiber
487 synapses have been revealed (Vyleta and Jonas, 2014; Vyleta et al., 2016; De Bruyckere et al., 2018;
488 Vandael et al., 2021a). Upon presynaptic activity, a detonating behavior can be observed in which a
489 limited number of – but not single – action potentials can elicit a suprathreshold postsynaptic
490 depolarisation (Henze et al., 2002a). Although this phenomenon has been extensively described in
491 mossy fiber bouton-CA3 pyramidal cell paired recordings (Vandael et al., 2021b), we were not able to
492 reveal detonating characteristics in granule cell-CA3 pyramidal cell pairs. We assume that both
493 differences in the experimental model and methodology can account for these differences, which
494 warrant further clarification in future studies. Nevertheless, a filtering of single action potentials with a
495 subsequent robust facilitation of synaptic transmission at this synapse was evident, which is in line with
496 previous reports (Zalutsky and Nicoll, 1990; Gundlfinger et al., 2007). Our results demonstrate that the
497 partial loss of input following lesion can influence both synaptic reliability and potency, which has been
498 observed for other plasticity-inducing stimuli at this synapse (Zalutsky and Nicoll, 1990). We suggest
499 that lesion-induced modulation of filtering/facilitation properties might interact with network
500 phenomena, such as pattern separation and completion along the dentate gyrus/CA3 axis. The increase
501 in synaptic reliability and potency might shift the balance towards pattern completion rather than
502 separation (O'Reilly and McClelland, 1994; Leutgeb et al., 2007; Prince et al., 2016). Moreover, the
503 presence of synaptopodin will presumably interfere with this network process under baseline and
504 plasticity-inducing conditions accounting for the previously reported cognitive deficits in synaptopodin-

505 deficient mice (Deller et al., 2003) and the synaptopodin-related cognitive decline during human aging
506 (Wingo et al., 2019).
507 Of note, it is an established view that mossy fiber synaptic plasticity is predominantly mediated by
508 presynaptic processes (Vandael et al., 2020; Orlando et al., 2021; Monday et al., 2022). Nevertheless,
509 recent work has suggested that the postsynaptic site shapes the transmission and plasticity through
510 transsynaptic mechanisms (Vandael et al., 2021a). In this study, we provide evidence that the
511 postsynaptically located spine apparatus organelle mediates denervation-induced synaptic plasticity at
512 this synapse. Since its discovery, the function of the spine apparatus organelle and the mechanisms
513 through which it orchestrates synaptic plasticity remained enigmatic. We here demonstrate that
514 synaptopodin and the spine apparatus organelle represent dendritic ribosomal hubs that contribute to
515 plasticity-driven local protein synthesis. The lesion-induced ultrastructural remodeling of the spine
516 apparatus organelle might therefore represent a novel regulatory mechanism for localized changes in
517 synaptic transmission (Vlachos et al., 2009; Dubes et al., 2022).
518 Notably, we found opposing plasticity phenomena at hippocampal mossy fiber synapses on the level of
519 individual neuron pairs in wildtype and synaptopodin-deficient tissue preparations. Synaptopodin
520 deficiency did not only cause defects in plasticity expression but hampered the ability of neurons to
521 maintain synaptic stability upon lesion. While the loss of input in wildtype cultures led to a significant
522 homeostatic strengthening of DG-CA3 excitatory synaptic transmission, synaptopodin deficiency was
523 associated with a lesion-related loss of synaptic potency. We therefore conclude that the function of the
524 spine apparatus organelle and its related protein synaptopodin might not be restricted to the mediation
525 of receptor accumulation at postsynaptic sites but rather comprises the implementation of plasticity
526 directionality (Vlachos, 2012). However, the link between synaptopodin and recently described
527 mechanisms that switch plasticity directionality from homeostatic to associative rules remain to be
528 determined (Wu et al., 2022). On the other hand, the lack of synaptopodin might decrease synaptic
529 resilience due to the lack of stabilizing features (Yap et al., 2020), which is required to maintain synaptic
530 transmission upon lesion. Regardless of these considerations, once more we report that synaptopodin
531 and the spine apparatus organelle act as crucial regulators of synaptic plasticity.
532 Finally, synaptic transcriptional changes as seen in wildtype cultures were absent in synaptopodin-
533 deficient cultures. Due to these observations, we suggest a dual role for synaptopodin as activity sensor
534 and plasticity effector, which assembles synapse-related mRNAs at dendritic plasticity hubs.

ACKNOWLEDGEMENTS

The Galaxy server that was used for some calculations in this study is partially funded by Collaborative Research Centre 992 Medical Epigenetics (DFG grant SFB 992/1 2012) and German Federal Ministry of Education and Research (BMBF grants 031 A538A/A538C RBC, 031L0101B/031L0101C de.NBI-epi, and 031L0106 de.STAIR (de.NBI)). We thank Bernd Heimrich for helpful and stimulating discussions on ultrastructural mossy fiber architecture. Moreover, we thank Sigrun Nestel for excellent technical assistance in electron microscopy. This work was supported by Else Kröner-Fresenius-Stiftung (EKFS_#2019_A94 to ML) and Deutsche Forschungsgemeinschaft (DFG; Project-ID 259373024 B14–CRC/TRR 167 to AV).

544 **REFERENCES**

545 Acsady L, Kamondi A, Sik A, Freund T, Buzsaki G (1998) GABAergic cells are the major postsynaptic targets of
546 mossy fibers in the rat hippocampus. J Neurosci 18:3386-3403.

547 Afgan E, Baker D, Batut B, van den Beek M, Bouvier D, Cech M, Chilton J, Clements D, Coraor N, Gruning BA,
548 Guerler A, Hillman-Jackson J, Hiltemann S, Jalili V, Rasche H, Soranzo N, Goecks J, Taylor J,
549 Nekrutenko A, Blankenberg D (2018) The Galaxy platform for accessible, reproducible and collaborative
550 biomedical analyses: 2018 update. Nucleic Acids Res 46:W537-W544.

551 Aoto J, Nam CI, Poon MM, Ting P, Chen L (2008) Synaptic signaling by all-trans retinoic acid in homeostatic
552 synaptic plasticity. Neuron 60:308-320.

553 Barnes SJ, Franzoni E, Jacobsen RI, Erdelyi F, Szabo G, Clopath C, Keller GB, Keck T (2017) Deprivation-
554 Induced Homeostatic Spine Scaling In Vivo Is Localized to Dendritic Branches that Have Undergone
555 Recent Spine Loss. Neuron 96:871-882 e875.

556 Batut B, van den Beek M, Doyle MA, Soranzo N (2021) RNA-Seq Data Analysis in Galaxy. Methods Mol Biol
557 2284:367-392.

558 Bissen D, Kracht MK, Foss F, Hofmann J, Acker-Palmer A (2021) EphrinB2 and GRIP1 stabilize mushroom
559 spines during denervation-induced homeostatic plasticity. Cell Rep 34:108923.

560 Chicurel ME, Harris KM (1992) Three-dimensional analysis of the structure and composition of CA3 branched
561 dendritic spines and their synaptic relationships with mossy fiber boutons in the rat hippocampus. J Comp
562 Neurol 325:169-182.

563 De Bruyckere E, Simon R, Nestel S, Heimrich B, Katzel D, Egorov AV, Liu P, Jenkins NA, Copeland NG,
564 Schwegler H, Draguhn A, Britsch S (2018) Stability and Function of Hippocampal Mossy Fiber Synapses
565 Depend on Bcl11b/Ctip2. Front Mol Neurosci 11:103.

566 Del Turco D, Deller T (2007) Organotypic entorhino-hippocampal slice cultures--a tool to study the molecular
567 and cellular regulation of axonal regeneration and collateral sprouting in vitro. Methods Mol Biol 399:55-
568 66.

569 Deller T, Korte M, Chabanis S, Drakew A, Schwegler H, Stefani GG, Zuniga A, Schwarz K, Bonhoeffer T, Zeller
570 R, Frotscher M, Mundel P (2003) Synaptopodin-deficient mice lack a spine apparatus and show deficits
571 in synaptic plasticity. Proc Natl Acad Sci U S A 100:10494-10499.

572 Dubes S, Soula A, Benquet S, Tessier B, Poujol C, Favereaux A, Thoumine O, Letellier M (2022) miR-124-
573 dependent tagging of synapses by synaptopodin enables input-specific homeostatic plasticity. EMBO
574 J:e109012.

575 Falahati H, Wu Y, Feuerer V, Simon HG, De Camilli P (2022) Proximity proteomics of synaptopodin provides
576 insight into the molecular composition of the spine apparatus of dendritic spines. Proc Natl Acad Sci U
577 S A 119:e2203750119.

578 Frotscher M, Heimrich B (1995) Lamina-specific synaptic connections of hippocampal neurons in vitro. J
579 Neurobiol 26:350-359.

580 Frotscher M, Heimrich B, Deller T (1997) Sprouting in the hippocampus is layer-specific. Trends Neurosci
581 20:218-223.

582 Frotscher M, Heimrich B, Deller T, Nitsch R (1995) Understanding the cortex through the hippocampus: lamina-
583 specific connections of the rat hippocampal neurons. J Anat 187 (Pt 3):539-545.

584 Galaxy C (2022) The Galaxy platform for accessible, reproducible and collaborative biomedical analyses: 2022
585 update. Nucleic Acids Res.

586 Goecks J, Nekrutenko A, Taylor J, Galaxy T (2010) Galaxy: a comprehensive approach for supporting accessible,
587 reproducible, and transparent computational research in the life sciences. Genome Biol 11:R86.

588 Gundlfinger A, Leibold C, Gebert K, Moisel M, Schmitz D, Kempter R (2007) Differential modulation of short-
589 term synaptic dynamics by long-term potentiation at mouse hippocampal mossy fibre synapses. J Physiol
590 585:853-865.

591 Haber M, Zhou L, Murai KK (2006) Cooperative astrocyte and dendritic spine dynamics at hippocampal excitatory
592 synapses. J Neurosci 26:8881-8891.

593 Heller JP, Rusakov DA (2017) The Nanoworld of the Tripartite Synapse: Insights from Super-Resolution
594 Microscopy. Front Cell Neurosci 11:374.

595 Hengen KB, Lambo ME, Van Hooser SD, Katz DB, Turrigiano GG (2013) Firing rate homeostasis in visual cortex
596 of freely behaving rodents. Neuron 80:335-342.

Henze DA, Wittner L, Buzsaki G (2002a) Single granule cells reliably discharge targets in the hippocampal CA3 network in vivo. Nat Neurosci 5:790-795.

Henze DA, McMahon DB, Harris KM, Barrionuevo G (2002b) Giant miniature EPSCs at the hippocampal mossy fiber to CA3 pyramidal cell synapse are monoquantal. J Neurophysiol 87:15-29.

Hulme SR, Jones OD, Raymond CR, Sah P, Abraham WC (2014) Mechanisms of heterosynaptic metaplasticity. Philos Trans R Soc Lond B Biol Sci 369:20130148.

Hunsaker MR, Rosenberg JS, Kesner RP (2008) The role of the dentate gyrus, CA3a,b, and CA3c for detecting spatial and environmental novelty. Hippocampus 18:1064-1073.

Jedlicka P, Deller T (2017) Understanding the role of synaptopodin and the spine apparatus in Hebbian synaptic plasticity - New perspectives and the need for computational modeling. Neurobiol Learn Mem 138:21-30.

Jedlicka P, Schwarzacher SW, Winkels R, Kienzler F, Frotscher M, Bramham CR, Schultz C, Bas Orth C, Deller T (2009) Impairment of in vivo theta-burst long-term potentiation and network excitability in the dentate gyrus of synaptopodin-deficient mice lacking the spine apparatus and the cisternal organelle. Hippocampus 19:130-140.

Korkotian E, Frotscher M, Segal M (2014) Synaptopodin regulates spine plasticity: mediation by calcium stores. J Neurosci 34:11641-11651.

Lambo ME, Turrigiano GG (2013) Synaptic and intrinsic homeostatic mechanisms cooperate to increase L2/3 pyramidal neuron excitability during a late phase of critical period plasticity. J Neurosci 33:8810-8819.

Lee KJ, Queenan BN, Rozeboom AM, Bellmore R, Lim ST, Vicini S, Pak DT (2013) Mossy fiber-CA3 synapses mediate homeostatic plasticity in mature hippocampal neurons. Neuron 77:99-114.

Lenz M, Galanis C, Kleidonas D, Fellenz M, Deller T, Vlachos A (2019) Denervated mouse dentate granule cells adjust their excitatory but not inhibitory synapses following in vitro entorhinal cortex lesion. Exp Neurol 312:1-9.

Lenz M, Kruse P, Eichler A, Straehle J, Beck J, Deller T, Vlachos A (2021a) All-trans retinoic acid induces synaptic plasticity in human cortical neurons. Elife 10.

Lenz M, Eichler A, Kruse P, Muellerleile J, Deller T, Jedlicka P, Vlachos A (2021b) All-trans retinoic acid induces synaptopodin-dependent metaplasticity in mouse dentate granule cells. Elife 10.

Lenz M, Eichler A, Kruse P, Strehl A, Rodriguez-Rozada S, Goren I, Yogev N, Frank S, Waisman A, Deller T, Jung S, Maggio N, Vlachos A (2020) Interleukin 10 Restores Lipopolysaccharide-Induced Alterations in Synaptic Plasticity Probed by Repetitive Magnetic Stimulation. Front Immunol 11:614509.

Leutgeb JK, Leutgeb S, Moser MB, Moser EI (2007) Pattern separation in the dentate gyrus and CA3 of the hippocampus. Science 315:961-966.

Lipp HP, Schwegler H, Heimrich B, Driscoll P (1988) Infrapyramidal mossy fibers and two-way avoidance learning: developmental modification of hippocampal circuitry and adult behavior of rats and mice. J Neurosci 8:1905-1921.

Maggio N, Vlachos A (2018) Tumor necrosis factor (TNF) modulates synaptic plasticity in a concentration-dependent manner through intracellular calcium stores. J Mol Med (Berl) 96:1039-1047.

Marr D (1971) Simple memory: a theory for archicortex. Philos Trans R Soc Lond B Biol Sci 262:23-81.

Maus L, Lee C, Altas B, Sertel SM, Weyand K, Rizzoli SO, Rhee J, Brose N, Imig C, Cooper BH (2020) Ultrastructural Correlates of Presynaptic Functional Heterogeneity in Hippocampal Synapses. Cell Rep 30:3632-3643 e3638.

Mesulam MM, Lalehzari N, Rahmani F, Ohm D, Shahidehpour R, Kim G, Gefen T, Weintraub S, Bigio E, Geula C (2019) Cortical cholinergic denervation in primary progressive aphasia with Alzheimer pathology. Neurology 92:e1580-e1588.

Monday HR, Kharod SC, Yoon YJ, Singer RH, Castillo PE (2022) Presynaptic FMRP and local protein synthesis support structural and functional plasticity of glutamatergic axon terminals. Neuron 110:2588-2606 e2586.

Mootha VK et al. (2003) PGC-1alpha-responsive genes involved in oxidative phosphorylation are coordinately downregulated in human diabetes. Nat Genet 34:267-273.

O'Reilly RC, McClelland JL (1994) Hippocampal conjunctive encoding, storage, and recall: avoiding a trade-off. Hippocampus 4:661-682.

649 Orlando M, Dvorzhak A, Bruentgens F, Maglione M, Rost BR, Sigrist SJ, Breustedt J, Schmitz D (2021)
650 Recruitment of release sites underlies chemical presynaptic potentiation at hippocampal mossy fiber
651 boutons. PLoS Biol 19:e3001149.

652 Platschek S, Cuntz H, Vuksic M, Deller T, Jedlicka P (2016) A general homeostatic principle following lesion
653 induced dendritic remodeling. Acta Neuropathol Commun 4:19.

654 Prang P, Del Turco D, Deller T (2003) Associational sprouting in the mouse fascia dentata after entorhinal lesion
655 in vitro. Brain Res 978:205-212.

656 Prince LY, Bacon TJ, Tigaret CM, Mellor JR (2016) Neuromodulation of the Feedforward Dentate Gyrus-CA3
657 Microcircuit. Front Synaptic Neurosci 8:32.

658 Raudvere U, Kolberg L, Kuzmin I, Arak T, Adler P, Peterson H, Vilo J (2019) g:Profiler: a web server for
659 functional enrichment analysis and conversions of gene lists (2019 update). Nucleic Acids Res 47:W191-
660 W198.

661 Reimand J, Isserlin R, Voisin V, Kucera M, Tannus-Lopes C, Rostamianfar A, Wadi L, Meyer M, Wong J, Xu C,
662 Merico D, Bader GD (2019) Pathway enrichment analysis and visualization of omics data using
663 g:Profiler, GSEA, Cytoscape and EnrichmentMap. Nat Protoc 14:482-517.

664 Robinson JL, Molina-Porcel L, Corrada MM, Raible K, Lee EB, Lee VM, Kawas CH, Trojanowski JQ (2014)
665 Perforant path synaptic loss correlates with cognitive impairment and Alzheimer's disease in the oldest-
666 old. Brain 137:2578-2587.

667 Shannon P, Markiel A, Ozier O, Baliga NS, Wang JT, Ramage D, Amin N, Schwikowski B, Ideker T (2003)
668 Cytoscape: a software environment for integrated models of biomolecular interaction networks. Genome
669 Res 13:2498-2504.

670 Strehl A, Galanis C, Radic T, Schwarzacher SW, Deller T, Vlachos A (2018) Dopamine Modulates Homeostatic
671 Excitatory Synaptic Plasticity of Immature Dentate Granule Cells in Entorhino-Hippocampal Slice
672 Cultures. Front Mol Neurosci 11:303.

673 Subramanian A, Tamayo P, Mootha VK, Mukherjee S, Ebert BL, Gillette MA, Paulovich A, Pomeroy SL, Golub
674 TR, Lander ES, Mesirov JP (2005) Gene set enrichment analysis: a knowledge-based approach for
675 interpreting genome-wide expression profiles. Proc Natl Acad Sci U S A 102:15545-15550.

676 Sutton MA, Ito HT, Cressy P, Kempf C, Woo JC, Schuman EM (2006) Miniature neurotransmission stabilizes
677 synaptic function via tonic suppression of local dendritic protein synthesis. Cell 125:785-799.

678 Tani H, Dulla CG, Farzampour Z, Taylor-Weiner A, Huguenard JR, Reimer RJ (2014) A local glutamate-
679 glutamine cycle sustains synaptic excitatory transmitter release. Neuron 81:888-900.

680 Thal DR, Holzer M, Rub U, Waldmann G, Gunzel S, Zedlick D, Schober R (2000) Alzheimer-related tau-
681 pathology in the perforant path target zone and in the hippocampal stratum oriens and radiatum correlates
682 with onset and degree of dementia. Exp Neurol 163:98-110.

683 Turrigiano G (2012) Homeostatic synaptic plasticity: local and global mechanisms for stabilizing neuronal
684 function. Cold Spring Harb Perspect Biol 4:a005736.

685 Turrigiano GG (2017) The dialectic of Hebb and homeostasis. Philos Trans R Soc Lond B Biol Sci 372.

686 Turrigiano GG, Leslie KR, Desai NS, Rutherford LC, Nelson SB (1998) Activity-dependent scaling of quantal
687 amplitude in neocortical neurons. Nature 391:892-896.

688 Vandael D, Okamoto Y, Jonas P (2021a) Transsynaptic modulation of presynaptic short-term plasticity in
689 hippocampal mossy fiber synapses. Nat Commun 12:2912.

690 Vandael D, Borges-Merjane C, Zhang X, Jonas P (2020) Short-Term Plasticity at Hippocampal Mossy Fiber
691 Synapses Is Induced by Natural Activity Patterns and Associated with Vesicle Pool Engram Formation.
692 Neuron 107:509-521 e507.

693 Vandael D, Okamoto Y, Borges-Merjane C, Vargas-Barroso V, Suter BA, Jonas P (2021b) Subcellular patch-
694 clamp techniques for single-bouton stimulation and simultaneous pre- and postsynaptic recording at
695 cortical synapses. Nat Protoc 16:2947-2967.

696 Viana da Silva S, Zhang P, Haberl MG, Labrousse V, Grosjean N, Blanchet C, Frick A, Mulle C (2019)
697 Hippocampal Mossy Fibers Synapses in CA3 Pyramidal Cells Are Altered at an Early Stage in a Mouse
698 Model of Alzheimer's Disease. J Neurosci 39:4193-4205.

699 Villanueva-Castillo C, Tecuatl C, Herrera-Lopez G, Galvan EJ (2017) Aging-related impairments of hippocampal
700 mossy fibers synapses on CA3 pyramidal cells. Neurobiol Aging 49:119-137.

701 Vitureira N, Letellier M, Goda Y (2012) Homeostatic synaptic plasticity: from single synapses to neural circuits.
702 Curr Opin Neurobiol 22:516-521.

703 Vlachos A (2012) Synaptopodin and the spine apparatus organelle-regulators of different forms of synaptic
704 plasticity? Ann Anat 194:317-320.

705 Vlachos A, Bas Orth C, Schneider G, Deller T (2012a) Time-lapse imaging of granule cells in mouse entorhino-
706 hippocampal slice cultures reveals changes in spine stability after entorhinal denervation. J Comp Neurol
707 520:1891-1902.

708 Vlachos A, Korkotian E, Schonfeld E, Copanaki E, Deller T, Segal M (2009) Synaptopodin regulates plasticity of
709 dendritic spines in hippocampal neurons. J Neurosci 29:1017-1033.

710 Vlachos A, Muller-Dahlhaus F, Rosskopp J, Lenz M, Ziemann U, Deller T (2012b) Repetitive magnetic
711 stimulation induces functional and structural plasticity of excitatory postsynapses in mouse organotypic
712 hippocampal slice cultures. J Neurosci 32:17514-17523.

713 Vlachos A, Becker D, Jedlicka P, Winkels R, Roeper J, Deller T (2012c) Entorhinal denervation induces
714 homeostatic synaptic scaling of excitatory postsynapses of dentate granule cells in mouse organotypic
715 slice cultures. PLoS One 7:e32883.

716 Vlachos A, Ikenberg B, Lenz M, Becker D, Reifenberg K, Bas-Orth C, Deller T (2013) Synaptopodin regulates
717 denervation-induced homeostatic synaptic plasticity. Proc Natl Acad Sci U S A 110:8242-8247.

718 Vyleta NP, Jonas P (2014) Loose coupling between Ca2+ channels and release sensors at a plastic hippocampal
719 synapse. Science 343:665-670.

720 Vyleta NP, Borges-Merjane C, Jonas P (2016) Plasticity-dependent, full detonation at hippocampal mossy fiber-
721 CA3 pyramidal neuron synapses. Elife 5.

722 Weng FJ, Garcia RI, Lutzu S, Alvina K, Zhang Y, Dushko M, Ku T, Zemoura K, Rich D, Garcia-Dominguez D,
723 Hung M, Yelhekar TD, Sorensen AT, Xu W, Chung K, Castillo PE, Lin Y (2018) Npas4 Is a Critical
724 Regulator of Learning-Induced Plasticity at Mossy Fiber-CA3 Synapses during Contextual Memory
725 Formation. Neuron 97:1137-1152 e1135.

726 Wingo AP, Dammer EB, Breen MS, Logsdon BA, Duong DM, Troncosco JC, Thambisetty M, Beach TG, Serrano
727 GE, Reiman EM, Caselli RJ, Lah JJ, Seyfried NT, Levey AI, Wingo TS (2019) Large-scale proteomic
728 analysis of human brain identifies proteins associated with cognitive trajectory in advanced age. Nat
729 Commun 10:1619.

730 Wu CH, Tatavarty V, Jean Beltran PM, Guerrero AA, Keshishian H, Krug K, MacMullan MA, Li L, Carr SA,
731 Cottrell JR, Turrigiano GG (2022) A bidirectional switch in the Shank3 phosphorylation state biases
732 synapses toward up- or downscaling. Elife 11.

733 Yap K, Drakew A, Smilovic D, Rietsche M, Paul MH, Vuksic M, Del Turco D, Deller T (2020) The actin-
734 modulating protein synaptopodin mediates long-term survival of dendritic spines. Elife 9.

735 Zalutsky RA, Nicoll RA (1990) Comparison of two forms of long-term potentiation in single hippocampal
736 neurons. Science 248:1619-1624.

737

FIGURES

Figure 1: Entorhinal cortex lesion caused homeostatic synaptic plasticity in both dentate granule cells and CA3 pyramidal cells.

(A) Entorhinal cortex lesion (ECL) in organotypic entorhino-hippocampal tissue cultures was performed by dissecting the perforant path (white line, scale bar 300 µm). Cytoarchitecture was visualized by DAPI nuclear staining.

(B) Spontaneous excitatory postsynaptic currents (sEPSCs) were recorded in both dentate granule cells and CA3 pyramidal cells in non-lesioned and lesioned cultures (3 days post lesion, 3 dp ECL).

(C-D) Spontaneous EPSC analysis in dentate granule cells revealed a lesion-induced excitatory synaptic strengthening in the mean sEPSC amplitude, half width and area (C; $n_{control}$ = 22 cells; $n_{3dp\ ECL}$ = 22 cells; Mann-Whitney test; Linear regression fit for XY-plot analysis). Percentile analysis of sEPSC amplitudes (D) demonstrated that the excitatory synaptic strengthening was evident in the 50% largest events (Mann-Whitney test).

(E-F) The frequency of sEPSCs was significantly increased 3 days after ECL (E; Mann-Whitney test). Moreover, amplitude/frequency-analysis shows that the abundance of larger sEPSC amplitudes was higher in lesioned cultures when compared to non-lesioned controls (F; RM-two-way ANOVA followed by Sidak's multiple comparisons test).

(G-H) Spontaneous EPSC analysis in CA3 pyramidal cells revealed a lesion-induced increase in mean sEPSC amplitude, whereas half width and area remained unchanged (G; $n_{control}$ = 48 cells; $n_{3dp\ ECL}$ = 49 cells; Mann-Whitney test; Linear regression fit for XY-plot analysis). Percentile analysis of sEPSC amplitudes (H) demonstrated that the excitatory synaptic strengthening was only visible in the 50% largest events (Mann-Whitney test).

(I-J) No lesion-induced changes in mean sEPSC frequency were detectable in CA3 pyramidal neurons. Amplitude/frequency-analysis showed a reduced number of small events in CA3 pyramidal cells 3 days after ECL (Mann-Whitney test for column statistics and RM-two-way ANOVA followed by Sidak's multiple comparisons test for XY-plot analysis).

Individual data points are indicated by colored dots. Values represent mean ± s.e.m (*$p < 0.05$, **$p < 0.01$, ***$p < 0.001$, ns - non significant difference).

766 **Figure 2: Entorhinal cortex lesion did not influence active or passive membrane properties.**
767 (A-B) Both resting membrane potential and input resistance (A) as well as the input-output curve for
768 the first 15 sweeps of current injection (B) in dentate granule cells were unaffected by ECL ($n_{control}$ = 22
769 cells; $n_{3dp\ ECL}$ = 22 cells; Mann-Whitney test and RM two-way ANOVA followed by Sidak's multiple
770 comparisons test for XY-plot analysis).
771 (C) Action potential frequency upon increasing current injection in dentate granule cells was similar in
772 non-lesioned and lesioned cultures (RM two-way ANOVA followed by Sidak's multiple comparisons
773 test).
774 (D-E) Both resting membrane potential and input resistance (D) as well as the input-output curve for
775 the first 15 sweeps of current injection (E) in CA3 pyramidal neurons were unaffected by the ECL
776 ($n_{control}$ = 48 cells; $n_{3dp\ ECL}$ = 49 cells; Mann-Whitney test and RM two-way ANOVA followed by Sidak's
777 multiple comparisons test for XY-plot analysis).
778 (F) Action potential frequency upon increasing current injection in CA3 pyramidal neurons is similar in
779 non-lesioned and lesioned cultures (RM two-way ANOVA followed by Sidak's multiple comparisons
780 test).

781 Individual data points are indicated by colored dots. Values represent mean ± s.e.m (ns - non significant
782 difference).

783 **Figure 3: Lesion-induced loss of the cortico-hippocampal projection changed transmission at**
784 **hippocampal mossy fiber synapses.**
785 (A) Post-hoc visualization of patched neurons in organotypic tissue cultures after paired-
786 electrophysiological recordings between individual presynaptic (pre) dentate granule cells and
787 postsynaptic (post) CA3 pyramidal neurons to analyze synaptic transmission features at hippocampal
788 mossy fiber synapses (scale bar 300 µm).
789 (B) Five consecutive action potentials were induced in dentate granule cells at 20 Hz (bottom trace) to
790 assess postsynaptic responses in CA3 pyramidal neurons in lesioned and non-lesioned cultures (upper
791 traces).
792 (C) The response rate, i.e., the fraction of presynaptic pulses that elicited a postsynaptic response in a
793 connected pair of individual neurons, was significantly increased for the first two pulses in lesioned
794 cultures when compared to non-lesioned controls ($n_{control}$ = 10; $n_{3dp\ ECL}$ = 10; Mann-Whitney test for the
795 respective pulse numbers).
796 (D) In successfully elicited unitary EPSCs (uEPSCs), a significant increase in uEPSC amplitude was
797 detectable ($n°1_{control}$ = 20 events, $n°1_{ECL}$ = 187 events; $n°2_{control}$ = 115 events, $n°2_{ECL}$ = 304 events;
798 $n°3_{control}$ = 292 events, $n°3_{ECL}$ = 394 events (one data point outside the axis limits); $n°4_{control}$ = 326 events,
799 $n°4_{ECL}$ = 385 events; $n°5_{control}$ = 307 events, $n°5_{ECL}$ = 384 events; Mann-Whitney test for the respective
800 pulse numbers).

801 Individual data points are indicated by colored dots. Values represent mean ± s.e.m (*$p < 0.05$, **$p <$
802 0.01, ***$p < 0.001$, ns - non significant difference).

Figure 4: The spine apparatus organelle assembles ribosomes and excitatory synapse related mRNAs.

(A) Transmission electron microscopy (TEM) images suggested a close association of ribosomes (arrowheads) and the spine apparatus organelle. Scale bar = 300 nm.

(B) Bioanalyzer traces (picoRNA Chip) from RNA samples prepared from precleared input (left) and Synpo-coIPs (right) demonstrating the co-immunoprecipitation of ribosomal RNA with anti-synaptopodin antibody. Notably, beads-only controls did not show an immunoprecipitation of rRNA.

(C) RT-qPCR analysis demonstrated a significant enrichment of Gria1 mRNA in synaptopodin-coIP compared to input samples indicating an association between the spine apparatus organelle and synaptic plasticity related mRNAs (normalized to Gapdh; $n_{input/SP\text{-}coIP} = 10$ samples, Mann-Whitney test).

(D) Analysis of differential mRNA abundance in Synpo-coIP RNA samples compared to their respective input samples to reveal the synaptopodin related transcriptome (extended data table 4-1). A log2(FC) value > 0 indicates an mRNA enrichment in Synpo-coIP samples (UP: 2355 genes; extended data table 4-2). Differentially enriched genes ($p_{adj.} < 0.05$) are indicated by orange dots (n = 5 samples input and Synpo-coIP respectively; 5-6 tissue cultures pooled from one filter per sample; DESeq2-analysis, usegalaxy.eu platform).

(E) A gene set enrichment analysis for a cellular compartment gene ontology was performed for significantly enriched genes in Synpo-coIP samples and visualized by a cytoscape map (node cutoff p = 0.05, edge cutoff (similarity): 0.8; node size reflects gene set size; node positions have been manually adjusted; original data set provided in extended data figure 4-3).

(F) Transmission electron microscopy was used to visualize ultrastructural properties of mossy fiber synapses in lesioned and non-lesioned control cultures (scale bar 1 µm).

(G) Upon lesion, the abundance of spine apparatus organelles (SA) and their number of dense plates were significantly increased in the postsynaptic compartment of mossy fiber synapses ($n_{control} = 120$ (no SA = 97 postsynapses, 1 dense plate = 22 postsynapses, 2 dense plates = 1 postsynapse, 3 dense plates = 0 postsynapses); $n_{ECL} = 90$ (no SA = 56 postsynapses, 1 dense plate = 21 postsynapses, 2 dense plates = 12 postsynapses, 3 dense plates = 1 postsynapses)).

(H) While the number of dense plates increased, their length significantly decreased 3 days after ECL ($n_{control} = 24$, one data point outside the axis limits; $n_{ECL} = 48$; Mann-Whitney test).

Individual data points are indicated by colored dots. Values represent mean ± s.e.m (**p < 0.01, ns - non significant difference).

834 **Figure 5: Entorhinal cortex lesion did not promote major changes in synaptopodin-associated**
835 **mRNA.**
836 Volcano plots to visualize the differential abundance of mRNAs in lesioned and non-lesioned cultures.
837 Both input and Synpo-coIP samples have been analyzed. Differentially expressed/enriched genes ($p_{adj.}$
838 < 0.05) are indicated by orange dots (n = 5 samples for both lesioned and non-lesioned cultures; 5-6
839 tissue cultures pooled from one filter per sample; DESeq2-analysis, usegalaxy.eu platform; extended
840 data tables 5-1 and 5-2).

841 **Figure 6: Lesion-induced homeostatic synaptic plasticity at hippocampal mossy fiber synapses**
842 **was impaired in synaptopodin-deficient tissue cultures.**
843 (A-B) sEPSCs were recorded from dentate granule cells in synaptopodin-deficient tissue cultures
844 (Synpo$^{-/-}$). Here, the mean sEPSC amplitude, half width and area significantly increased 3 days after the
845 ECL (A; $n_{control}$ = 29; $n_{3dp\ ECL}$ = 26; Mann-Whitney test; Linear regression fit for XY-plot analysis). In
846 contrast to wildtype cultures, no changes in the mean sEPSC frequency or the sEPSC
847 amplitude/frequency-distribution were observed (B; Mann-Whitney test for column statistics and RM-
848 two-way ANOVA followed by Sidak's multiple comparisons test for XY-plot analysis).
849 (C) No changes in passive membrane properties of dentate granule cells were detected in synaptopodin-
850 deficient cultures upon lesion (Mann-Whitney test for column statistics and RM-two-way ANOVA
851 followed by Sidak's multiple comparisons test for XY-plot analysis).
852 (D-E) The mean sEPSC amplitude in CA3 pyramidal neurons was not significantly different in lesioned
853 and non-lesioned control cultures. Noteworthy, the mean sEPSC half width significantly decreased in
854 lesioned cultures (D; $n_{control}$ = 25; $n_{3dp\ ECL}$ = 25; Mann-Whitney test; linear regression fit for XY-plot
855 analysis). No lesion-induced changes in the mean sEPSC frequency or the amplitude/frequency-
856 interdependence were detectable (E; Mann-Whitney test for column statistics and RM-two-way
857 ANOVA followed by Sidak's multiple comparisons test for XY-plot analysis).
858 (F) No changes in passive membrane properties of CA3 pyramidal neurons were detected in
859 synaptopodin-deficient cultures upon lesion (Mann-Whitney test for column statistics and RM-two-way
860 ANOVA followed by Sidak's multiple comparisons test for XY-plot analysis).
861 (G-H) Paired whole-cell patch-clamp recordings were carried out between individual dentate granule
862 cells (GC) and CA3 pyramidal neurons in lesioned and non-lesioned control cultures prepared from
863 synaptopodin-deficient animals (G). Upon injection of 5 current pulses in the presynaptic granule cells,
864 no changes in the pulse-number-dependent response rate of connected mossy fiber synapses were
865 detectable after the ECL (H; $n_{control}$ = 12; $n_{3dp\ ECL}$ = 10; Mann-Whitney test for the respective pulse
866 numbers).
867 (I) Analyzing properties of successfully transmitted uEPSCs, a significant decrease in uEPSC amplitude
868 was evident in lesioned cultures when compared to non-lesioned controls ($n°1_{control}$ = 144 events, $n°1_{ECL}$
869 = 82 events; $n°2_{control}$ = 300 events, $n°2_{ECL}$ = 263 events; $n°3_{control}$ = 426 events (one data point outside
870 the axis limits), $n°3_{ECL}$ = 402 events; $n°4_{control}$ = 486 events, $n°4_{ECL}$ = 364 events; $n°5_{control}$ = 472 events,
871 $n°5_{ECL}$ = 317 events; Mann-Whitney test for the respective pulse numbers).

872 Individual data points are indicated by colored dots. Values represent mean ± s.e.m (*$p < 0.05$, ***$p <$
873 0.001, ns - non significant difference).

874 **Figure 7: Synaptopodin deficiency shifted the hippocampal mossy fiber synapse to an excitable**
875 **state under baseline conditions.**
876 (A-B) sEPSCs from CA3 pyramidal cells of both synaptopodin-deficient and wildtype tissue
877 preparations respectively. While the mean sEPSC amplitude was unchanged, sEPSC area and half width
878 were significantly increased in synaptopodin-deficient tissue cultures (A; $n_{Synpo+/+} = 48$; $n_{Synpo-/-} = 25$;
879 Mann-Whitney test; Linear regression fit for XY-plot analysis). Additionally, the sEPSC
880 amplitude/frequency-distribution was significantly changed between the two groups (B; RM-two-way
881 ANOVA followed by Sidak's multiple comparisons test).
882 (C-D) When comparing the response rate of postsynaptic CA3 neurons upon presynaptic action
883 potential generation from paired recordings in $Synpo^{+/+}$ and $Synpo^{-/-}$ tissue preparations, no significant
884 increase was observed (C; $n_{Synpo+/+} = 10$; $n_{Synpo-/-} = 12$; Mann-Whitney test for the respective pulse
885 numbers; c.f., Figures 3 and 6). However, when analyzing the amplitudes of successfully transmitted
886 uEPSCs at the postsynaptic CA3 pyramidal cells, a significant increase in uEPSC amplitudes became
887 evident in synaptopodin-deficient tissue preparations after each of the five pulses respectively (D;
888 $n°1_{Synpo+/+} = 20$ events, $n°1_{Synpo-/-} = 144$ events; $n°2_{Synpo+/+} = 115$ events, $n°2_{Synpo-/-} = 300$ events; $n°3_{Synpo+/+}$
889 $= 292$ events, $n°3_{Synpo-/-} = 426$ events (one data point outside the axis limits); $n°4_{Synpo+/+} = 326$ events,
890 $n°4_{Synpo-/-} = 486$ events; $n°5_{Synpo+/+} = 307$ events, $n°5_{Synpo-/-} = 472$ events; Mann-Whitney test for the
891 respective pulse numbers).

892 Individual data points are indicated by colored dots. Values represent mean ± s.e.m (*$p < 0.05$, **$p <$
893 0.01, ***$p < 0.001$, ns - non significant difference).

894 **Figure 8: Entorhinal cortex lesion induced synaptopodin-dependent transcriptomic changes.**
895 (A) Volcano Plots to visualize differential gene expression in wildtype (Synpo$^{+/+}$) and synaptopodin-
896 deficient (Synpo$^{-/-}$) tissue preparations based on region-specific transcriptome analysis of the dentate
897 gyrus and the CA3 area. Colored dots indicate differentially expressed genes ($p_{adj.} < 0.05$; CA3-Synpo$^{+/+}$:
898 $n_{control} = 2$, $n_{3dpECL} = 3$; DG-Synpo$^{+/+}$: $n_{control} = 4$, $n_{3dpECL} = 7$; CA3-Synpo$^{-/-}$: $n_{control} = 6$, $n_{3dpECL} = 6$; DG-
899 Synpo$^{-/-}$: $n_{control} = 7$, $n_{3dpECL} = 4$; detailed DESeq2-outputs provided in extended data table 8-1, 8-2, 8-3
900 and 8-4).
901 (B) VENN-diagrams illustrate the magnitude of lesion-induced differential gene expression and the
902 overlap in commonly regulated genes between wildtype and synaptopodin-deficient tissue preparations.
903 Synaptopodin-deficient preparations showed deficits in lesion-induced gene expression mainly in the
904 CA3 region. Despite the identification of commonly regulated genes, a considerable number of
905 genotype-specific changes can be identified in DG samples.
906 (C) For wildtype CA3 samples (Synpo$^{+/+}$-CA3), a gene set enrichment analysis (gene ontologies:
907 molecular function (MF) and cellular compartment (CC)) was performed and visualized (TOP-5) by the
908 g:Profiler web platform.
909 (D) Heatmap-visualization demonstrates the differential expression of synapse related genes (GOCC:
910 0045202) upon lesion-induced cellular remodeling in the wildtype CA3 region. TOP-10 differentially
911 expressed genes were additionally illustrated.
912 (E) For wildtype DG samples (Synpo$^{+/+}$-DG), a gene set enrichment analysis (gene ontologies:
913 molecular function (MF) and cellular compartment (CC)) was performed and visualized (TOP-5) by the
914 g:Profiler web platform.
915 (F) Heatmap-visualization demonstrates the differential expression of synapse related genes (GOCC:
916 0045202) upon lesion-induced cellular remodeling in the wildtype DG region. TOP-10 differentially
917 expressed genes for both UP and DOWN regulation were additionally illustrated.

918 Analysis was performed on the Galaxy platform, Differential gene expression was determined using the
919 DESeq2 application.

920 **EXTENDED DATA TABLES**

921 Extended data table 4-1: DESeq2 results table Synpo-coIP vs. input (BaseMean > 300; c.f. Fig. 4)

922 Extended data table 4-2: Synpo-coIP enriched genes (log2FC > 0; c.f. Fig. 4)

923 Extended data figure 4-3: Cytoscape map from Synpo-coIP enrichment experiments (c.f. Fig. 4)

924 Extended data table 5-1: DESeq2 results table ECL vs. control (input; Base Mean > 300; c.f. Figure 5)

925 Extended data table 5-2: DESeq2 results table ECL vs. control (Synpo-coIP; Base Mean > 300; c.f.
926 Figure 5)

927 Extended data table 8-1: DESeq2 results table ECL vs. control (Synpo$^{+/+}$, CA3; Base Mean > 300; c.f.
928 Figure 8)

929 Extended data table 8-2: DESeq2 results table ECL vs. control (Synpo$^{+/+}$, DG; Base Mean > 300; c.f.
930 Figure 8)

931 Extended data table 8-3: DESeq2 results table ECL vs. control (Synpo$^{-/-}$, CA3; Base Mean > 300; c.f.
932 Figure 8)

933 Extended data table 8-4: DESeq2 results table ECL vs. control (Synpo$^{-/-}$, DG; Base Mean > 300; c.f.
934 Figure 8)

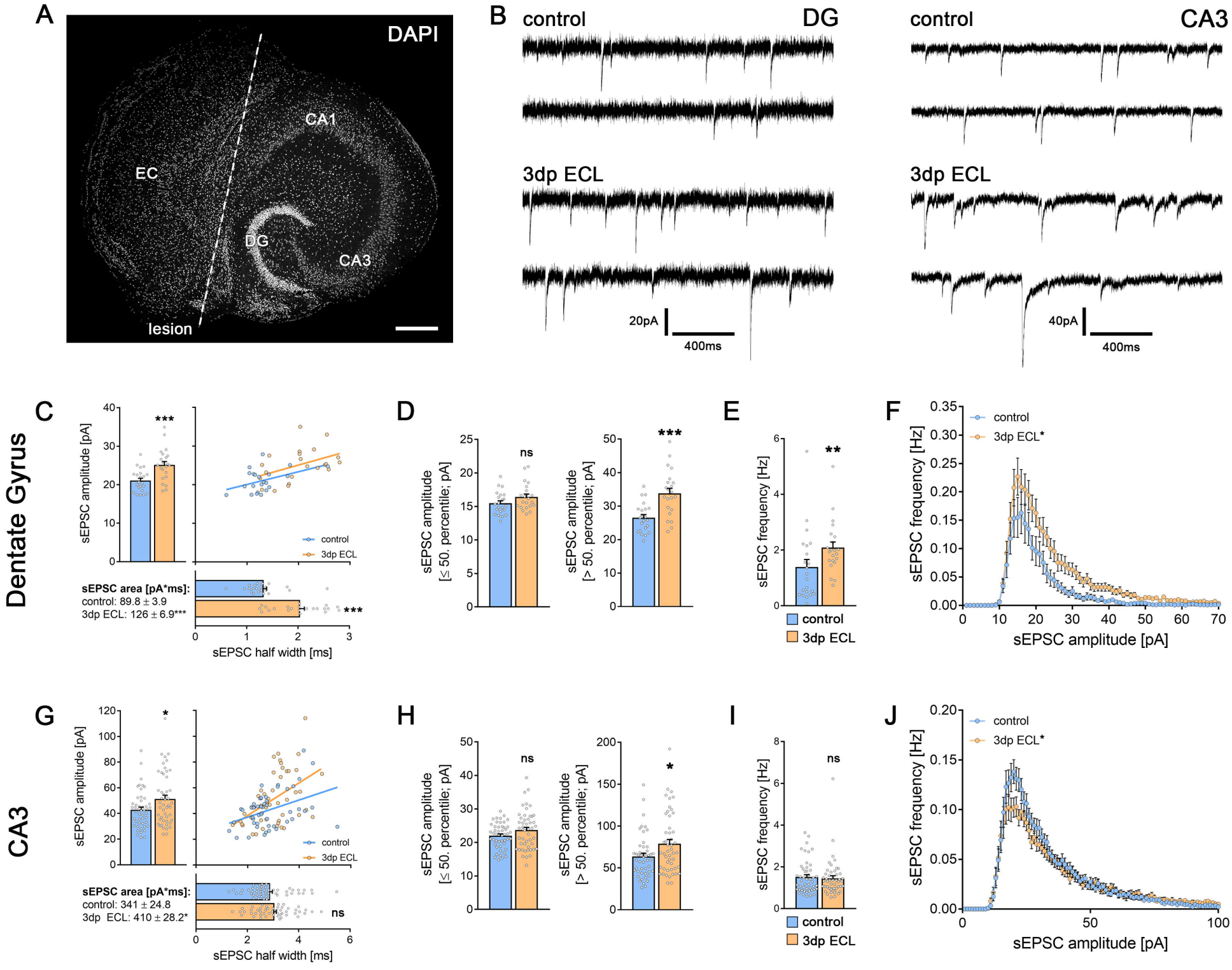
A
DAPI
CA1
EC
DG
CA3
lesion
B
control
DG
3dp ECL
20pA
400ms
control
CA3
3dp ECL
40pA
400ms
Dentate Gyrus
C
sEPSC amplitude [pA]
***
control
3dp ECL
sEPSC area [pA*ms]:
control: 89.8 ± 3.9
3dp ECL: 126 ± 6.9***
***
sEPSC half width [ms]
D
sEPSC amplitude [≤ 50. percentile; pA]
ns
sEPSC amplitude [> 50. percentile; pA]
***
E
sEPSC frequency [Hz]
**
control
3dp ECL
F
sEPSC frequency [Hz]
control
3dp ECL*
sEPSC amplitude [pA]
CA3
G
sEPSC amplitude [pA]
*
control
3dp ECL
sEPSC area [pA*ms]:
control: 341 ± 24.8
3dp ECL: 410 ± 28.2*
ns
sEPSC half width [ms]
H
sEPSC amplitude [≤ 50. percentile; pA]
ns
sEPSC amplitude [> 50. percentile; pA]
*
I
sEPSC frequency [Hz]
ns
control
3dp ECL
J
sEPSC frequency [Hz]
control
3dp ECL*
sEPSC amplitude [pA]

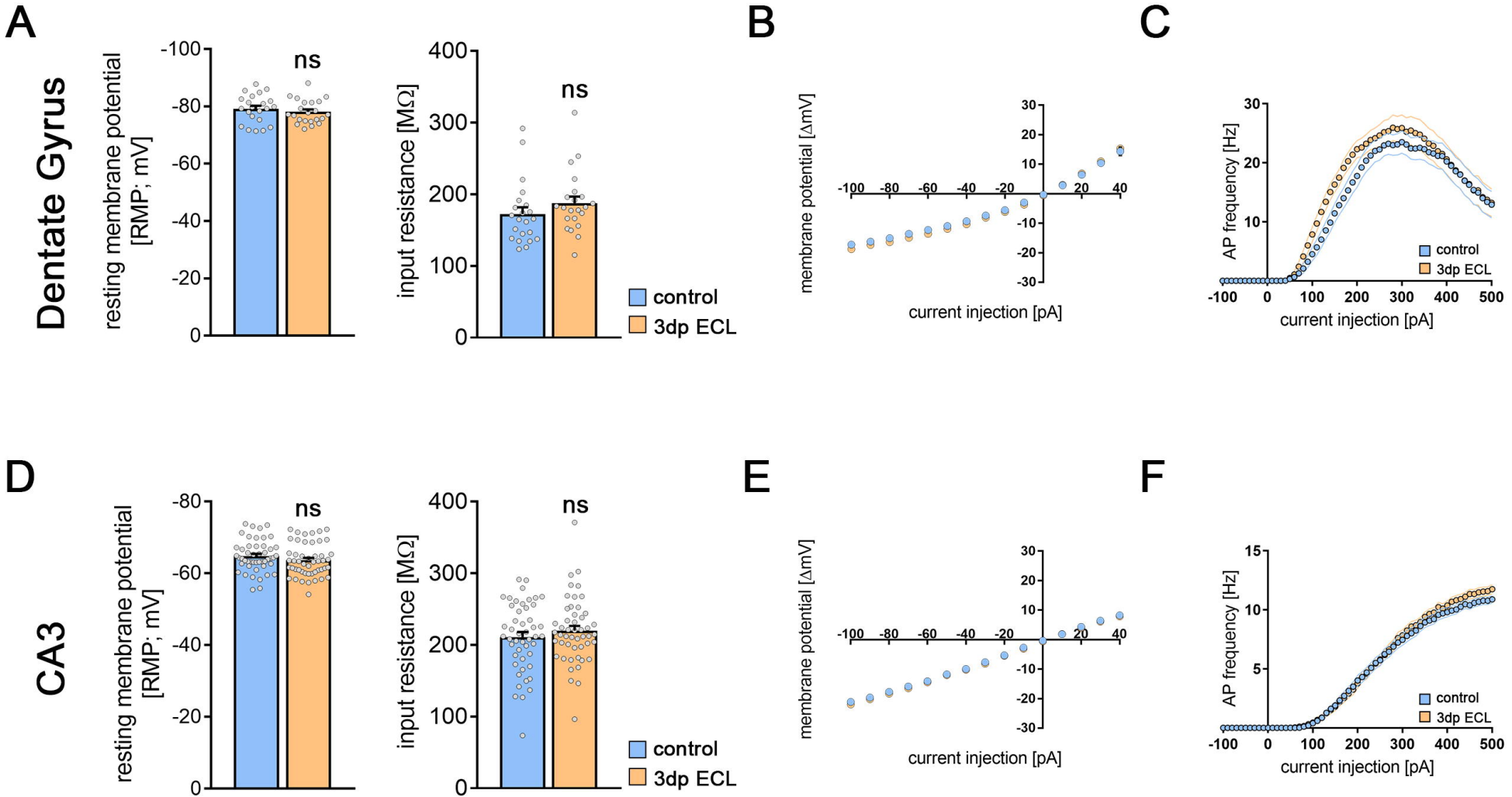
A
Dentate Gyrus
resting membrane potential [RMP; mV]
-100
-80
-60
-40
-20
0
ns
input resistance [MΩ]
400
300
200
100
0
ns
control
3dp ECL
B
membrane potential [ΔmV]
30
20
10
-10
-20
-30
-100
-80
-60
-40
-20
20
40
current injection [pA]
C
AP frequency [Hz]
30
20
10
-100
0
100
200
300
400
500
current injection [pA]
control
3dp ECL
D
CA3
resting membrane potential [RMP; mV]
-80
-60
-40
-20
0
ns
input resistance [MΩ]
400
300
200
100
0
ns
control
3dp ECL
E
membrane potential [ΔmV]
30
20
10
-10
-20
-30
-100
-80
-60
-40
-20
20
40
current injection [pA]
F
AP frequency [Hz]
15
10
5
-100
0
100
200
300
400
500
current injection [pA]
control
3dp ECL

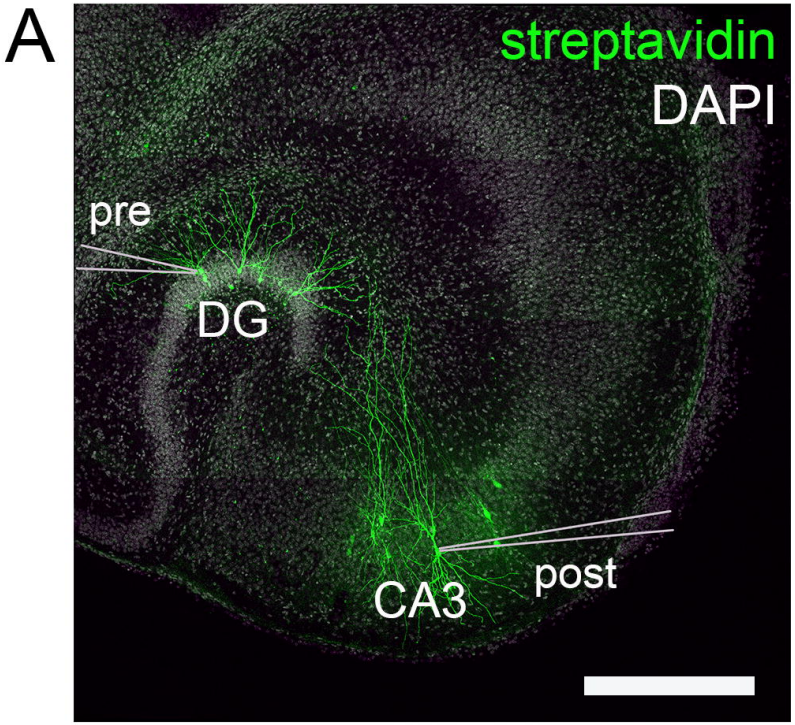
A
streptavidin
DAPI
pre
DG
CA3
post

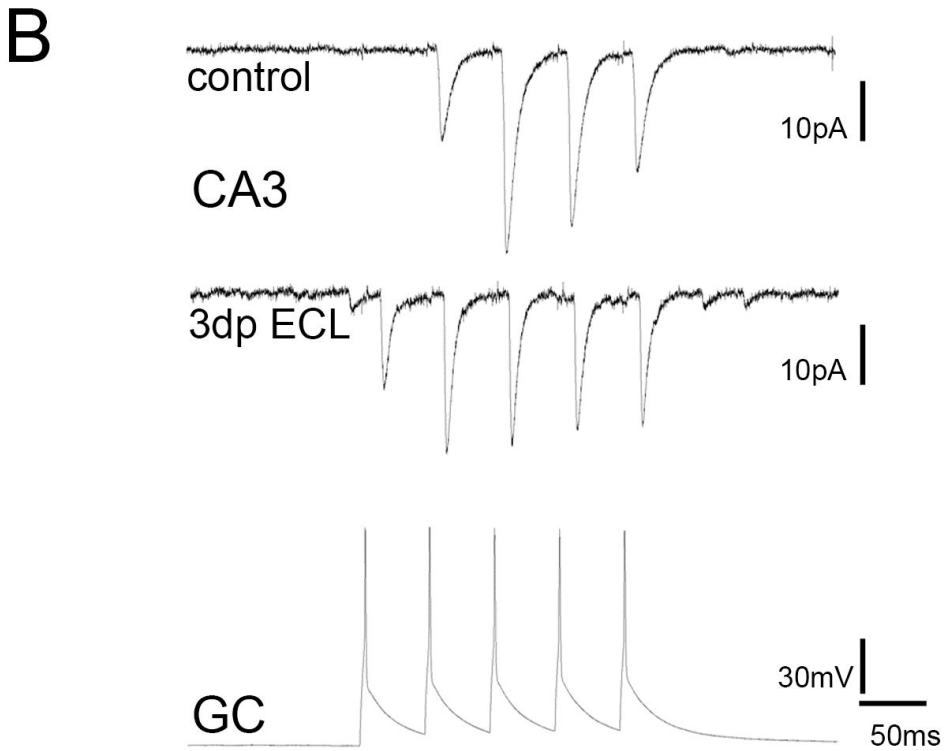
B
control
10pA
CA3
3dp ECL
10pA
30mV
GC
50ms

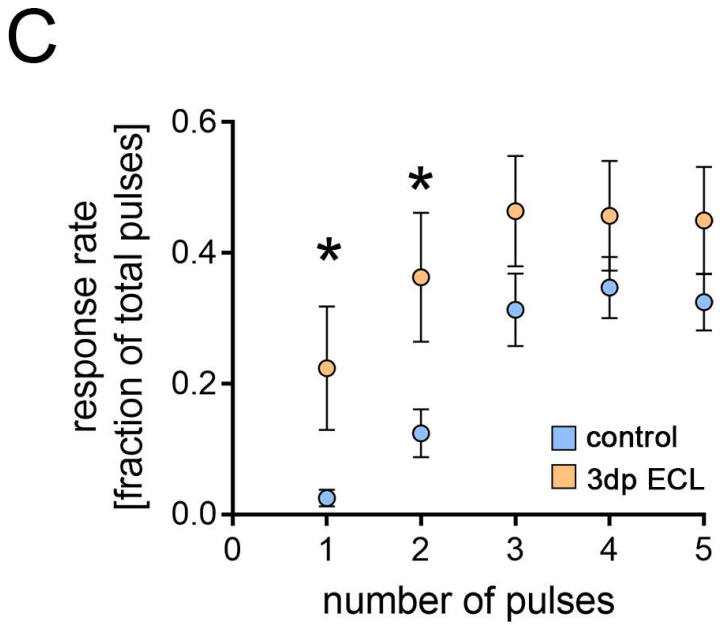
C
response rate
[fraction of total pulses]
0.6
0.4
0.2
0.0
0
1
2
3
4
5
number of pulses
*
*
control
3dp ECL

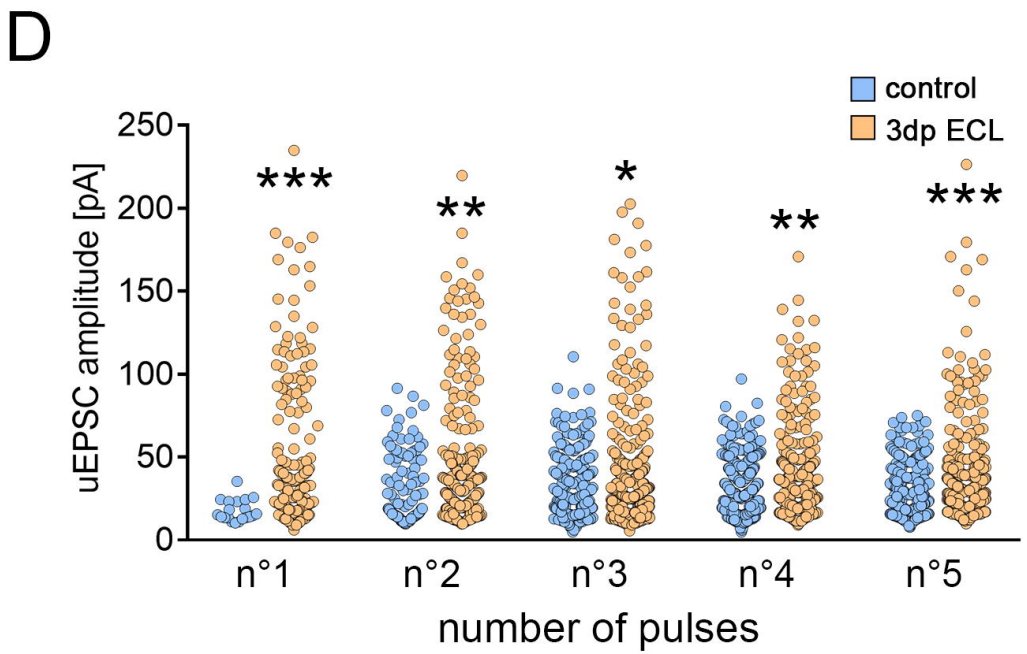
D
control
3dp ECL
uEPSC amplitude [pA]
250
200
150
100
50
0
***
**
*
**
***
n°1
n°2
n°3
n°4
n°5
number of pulses

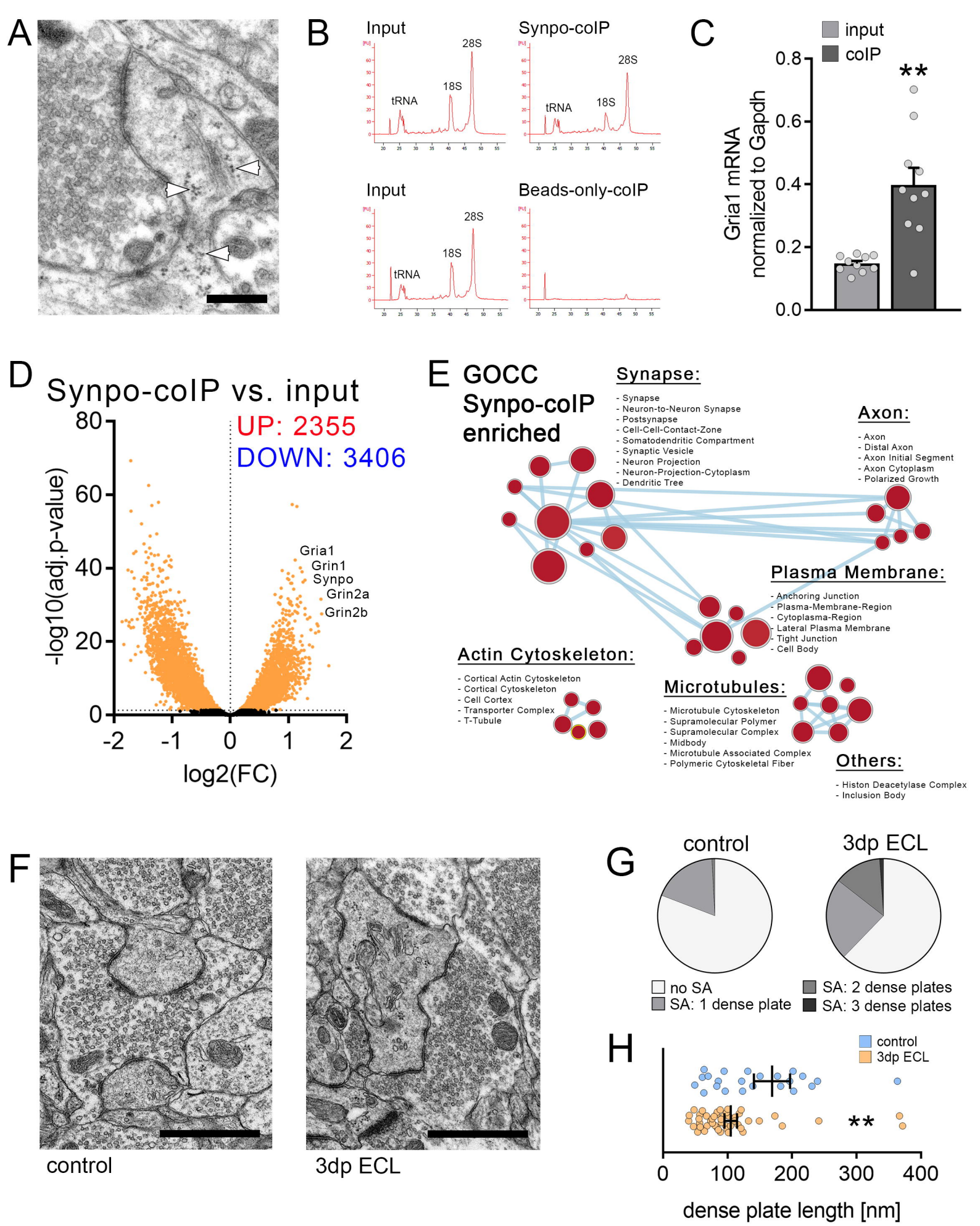
A
B
Input
Synpo-coIP
28S
18S
tRNA
Input
Beads-only-coIP
C
input
coIP
Gria1 mRNA normalized to Gapdh
0.0
0.2
0.4
0.6
0.8
**
D
Synpo-coIP vs. input
UP: 2355
DOWN: 3406
-log10(adj.p-value)
log2(FC)
Gria1
Grin1
Synpo
Grin2a
Grin2b
E
GOCC Synpo-coIP enriched
Synapse:
- Synapse
- Neuron-to-Neuron Synapse
- Postsynapse
- Cell-Cell-Contact-Zone
- Somatodendritic Compartment
- Synaptic Vesicle
- Neuron Projection
- Neuron-Projection-Cytoplasm
- Dendritic Tree
Axon:
- Axon
- Distal Axon
- Axon Initial Segment
- Axon Cytoplasm
- Polarized Growth
Plasma Membrane:
- Anchoring Junction
- Plasma-Membrane-Region
- Cytoplasma-Region
- Lateral Plasma Membrane
- Tight Junction
- Cell Body
Actin Cytoskeleton:
- Cortical Actin Cytoskeleton
- Cortical Cytoskeleton
- Cell Cortex
- Transporter Complex
- T-Tubule
Microtubules:
- Microtubule Cytoskeleton
- Supramolecular Polymer
- Supramolecular Complex
- Midbody
- Microtubule Associated Complex
- Polymeric Cytoskeletal Fiber
Others:
- Histon Deacetylase Complex
- Inclusion Body
F
control
3dp ECL
G
control
3dp ECL
no SA
SA: 1 dense plate
SA: 2 dense plates
SA: 3 dense plates
H
control
3dp ECL
**
0
100
200
300
400
dense plate length [nm]

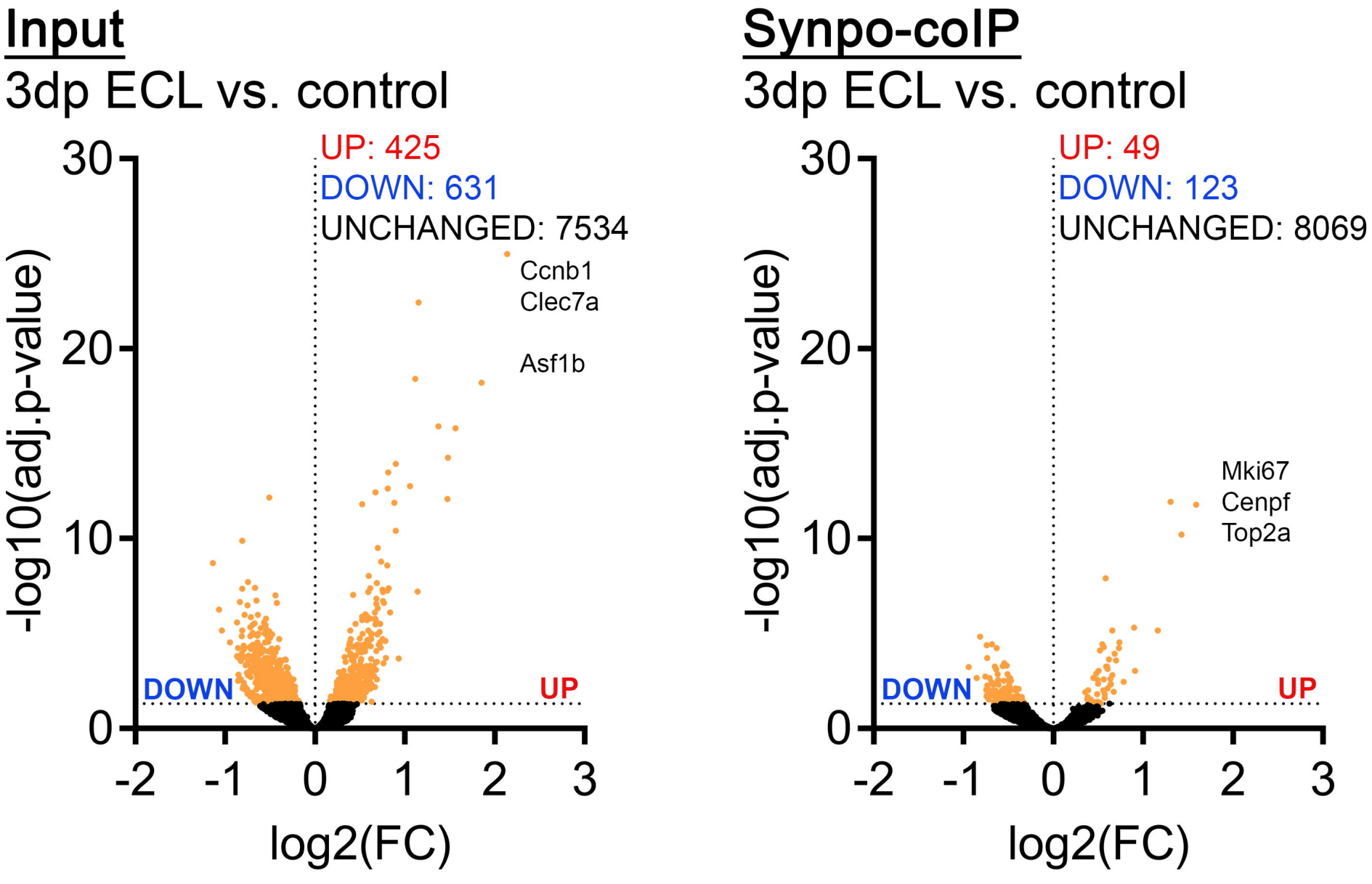
Input
3dp ECL vs. control
UP: 425
DOWN: 631
UNCHANGED: 7534
Ccnb1
Clec7a
Asf1b
DOWN
UP
-log10(adj.p-value)
log2(FC)
Synpo-coIP
3dp ECL vs. control
UP: 49
DOWN: 123
UNCHANGED: 8069
Mki67
Cenpf
Top2a
DOWN
UP
-log10(adj.p-value)
log2(FC)

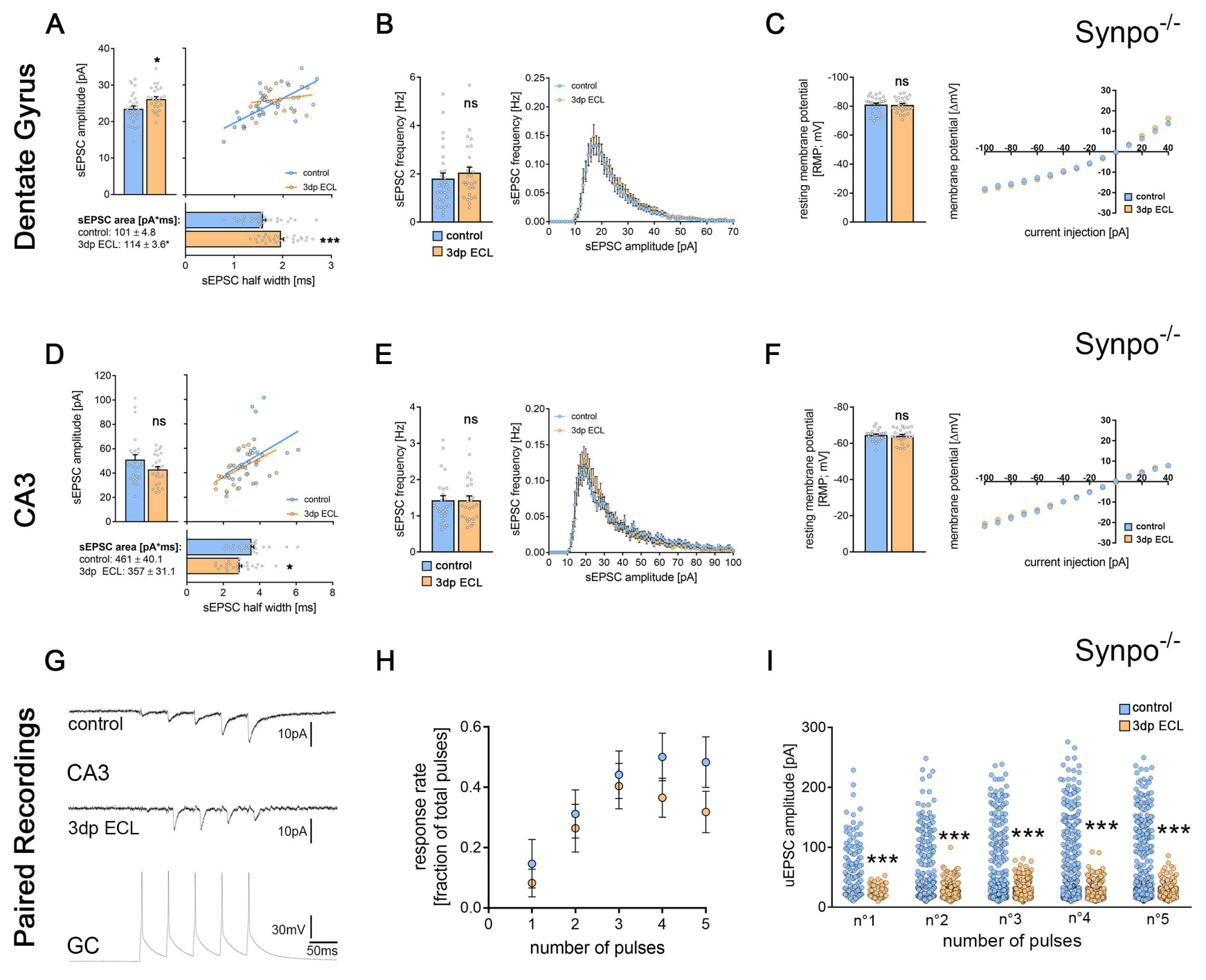
Dentate Gyrus
A
sEPSC amplitude [pA]
*
control
3dp ECL
sEPSC area [pA*ms]:
control: 101 ± 4.8
3dp ECL: 114 ± 3.6*
***
sEPSC half width [ms]
B
sEPSC frequency [Hz]
ns
control
3dp ECL
sEPSC amplitude [pA]
C
Synpo-/-
resting membrane potential [RMP; mV]
ns
membrane potential [ΔmV]
current injection [pA]
CA3
D
sEPSC amplitude [pA]
ns
sEPSC area [pA*ms]:
control: 461 ± 40.1
3dp ECL: 357 ± 31.1
*
sEPSC half width [ms]
E
sEPSC frequency [Hz]
ns
sEPSC amplitude [pA]
F
Synpo-/-
resting membrane potential [RMP; mV]
ns
membrane potential [ΔmV]
current injection [pA]
Paired Recordings
G
control
10pA
CA3
3dp ECL
10pA
30mV
50ms
GC
H
response rate [fraction of total pulses]
number of pulses
I
Synpo-/-
control
3dp ECL
uEPSC amplitude [pA]
***
n°1
n°2
n°3
n°4
n°5
number of pulses

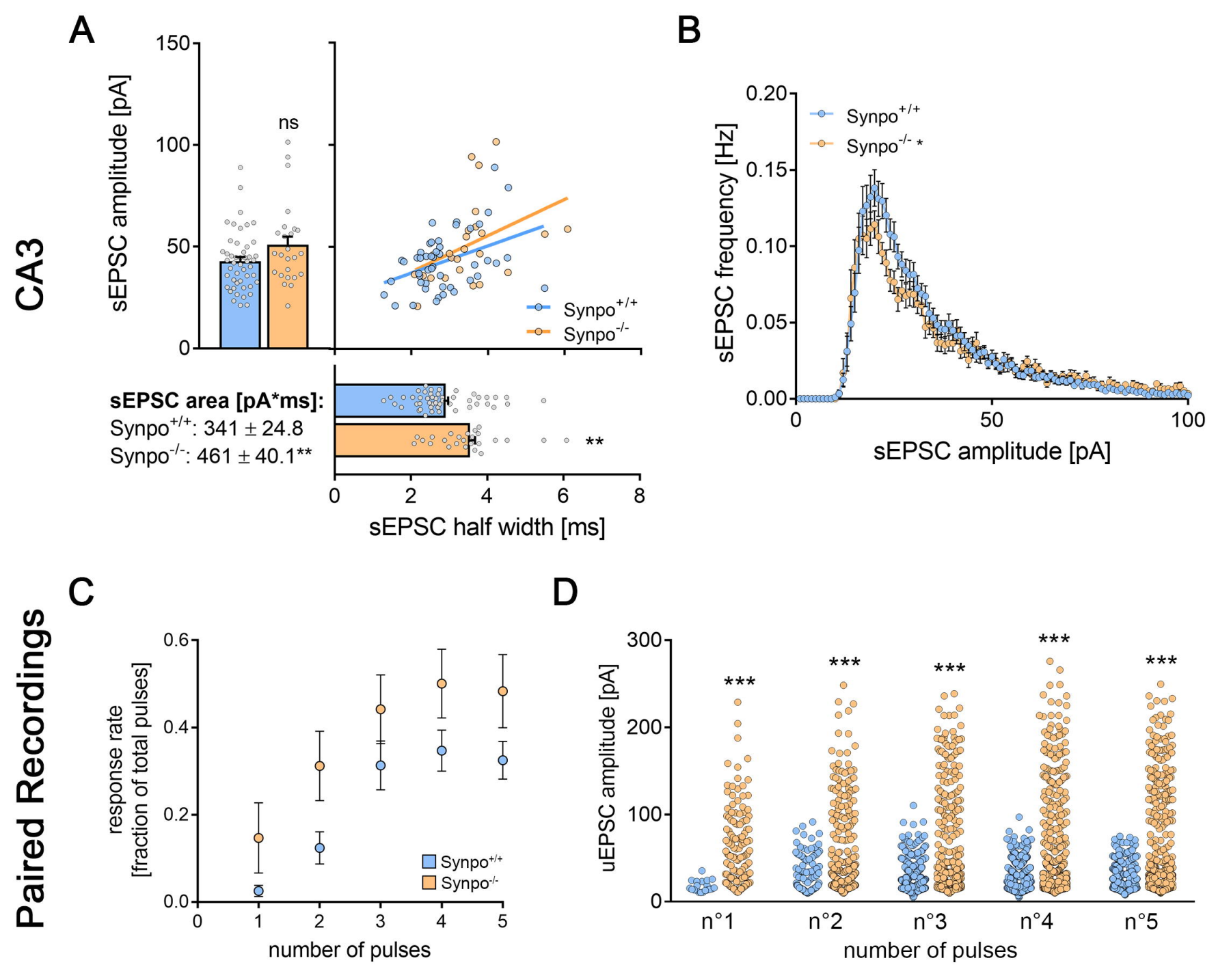
A
CA3
sEPSC amplitude [pA]
150
100
50
0
ns
Synpo+/+
Synpo-/-
sEPSC area [pA*ms]:
Synpo+/+: 341 ± 24.8
Synpo-/-: 461 ± 40.1**
**
0
2
4
6
8
sEPSC half width [ms]
B
sEPSC frequency [Hz]
0.20
0.15
0.10
0.05
0.00
Synpo+/+
Synpo-/- *
0
50
100
sEPSC amplitude [pA]
Paired Recordings
C
response rate
[fraction of total pulses]
0.6
0.4
0.2
0.0
Synpo+/+
Synpo-/-
0
1
2
3
4
5
number of pulses
D
uEPSC amplitude [pA]
300
200
100
0
***
n°1
n°2
n°3
n°4
n°5
number of pulses

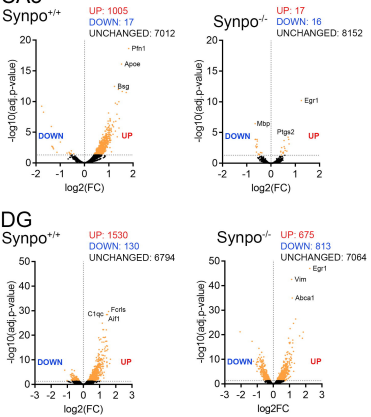

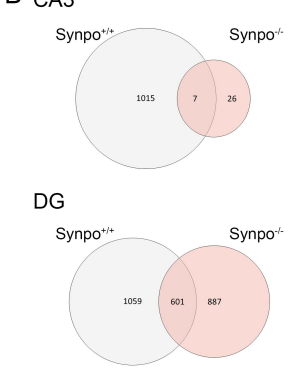

C Synpo$^{+/+}$ - CA3

GO:MF		stats	
Term name	Term ID	p_{adj}	$-\log_{10}(p_{adj})$ (0 – >16)
ubiquitin-like protein ligase binding	GO:0044389	2.482×10^{-10}	
ubiquitin protein ligase binding	GO:0031625	6.168×10^{-10}	
GTP binding	GO:0005525	1.490×10^{-8}	
guanyl nucleotide binding	GO:0019001	1.034×10^{-7}	
guanyl ribonucleotide binding	GO:0032561	1.034×10^{-7}	

GO:CC		stats	
Term name	Term ID	p_{adj}	$-\log_{10}(p_{adj})$ (0 – >16)
exocytic vesicle	GO:0070382	2.324×10^{-19}	
synaptic vesicle	GO:0008021	3.544×10^{-19}	
transport vesicle	GO:0030133	6.265×10^{-19}	
myelin sheath	GO:0043209	3.399×10^{-17}	
glutamatergic synapse	GO:0098978	3.857×10^{-13}	

D CA3 - GO:Synapse

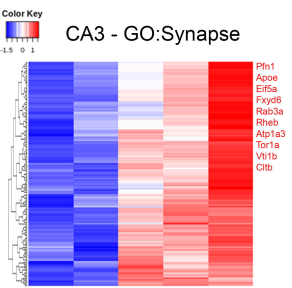

E Synpo$^{+/+}$ - DG

GO:MF		stats	
Term name	Term ID	p_{adj}	$-\log_{10}(p_{adj})$ (0 – >16)
actin binding	GO:0003779	1.175×10^{-8}	
ubiquitin-like protein ligase binding	GO:0044389	1.162×10^{-7}	
ubiquitin protein ligase binding	GO:0031625	4.309×10^{-7}	
GTP binding	GO:0005525	4.205×10^{-4}	
DNA-binding transcription factor binding	GO:0140297	9.194×10^{-4}	

GO:CC		stats	
Term name	Term ID	p_{adj}	$-\log_{10}(p_{adj})$ (0 – >16)
endosome membrane	GO:0010008	1.049×10^{-12}	
cell leading edge	GO:0031252	5.334×10^{-12}	
mitochondrial matrix	GO:0005759	5.413×10^{-12}	
peptidase complex	GO:1905368	1.144×10^{-11}	
endopeptidase complex	GO:1905369	1.217×10^{-11}	
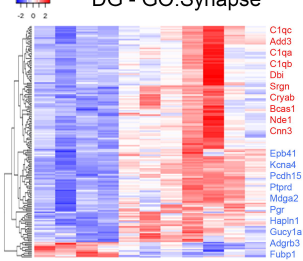
F DG - GO:Synapse